Università
Ca'Foscari
Venezia

Master's Degree
in
Science and
Technology of Bio and
Nanomaterials

Final Thesis

# First-Principles Investigation of Doped BaTiO$_3$-based Perovskite Systems

**Supervisor**
Ch. Prof. Andrea Pietropolli Charmet

**Graduand**
Tommaso Francese
Matriculation number
818936

**Academic Year**
2021 / 2022

"Data! Data! Data!" he cried impatiently. "I can't make bricks without clay." -
Arthur Conan Doyle, *The Adventure of the Copper Beeches*

# Abstract

The intriguing nature of the $BaTiO_3$ perovskite system has been largely debated and investigated in recent years thanks to its intrinsic properties like high visible-light absorption coefficients, high photoluminescence quantum yield, long charge carrier diffusion length, colossal magnetoresistance, superconductivity, and many other interesting and valuable solid-state properties. The general application of the perovskite systems covers a wide range of technological devices and solutions that are foreseen to be part of the next future general technological advancement. In this perspective, our work focuses on the ab initio prediction of the basic properties of a subset of $BaTiO_3$-based perovskite models which display different doping rates ranging from 25% to 50%. These doping are performed by replacing Titanium (Ti) with Tin (Sn) (50% substitution) and Barium (Ba) with Strontium (Sr) (25 and 50% substitution), paving the way for more complex modifications required to engineer the intrinsic properties of the studied systems, such as band structure, density of states, bulk modules etc.

# Contents

# List of Figures

# List of Tables

# Chapter 1

# Introduction

In this introductory chapter, a brief assessment of the origins of $BaTiO_3$ system and its properties is presented, together with some historical facts that made possibile its synthesis, development and successive study. The phase transition diagram of the system is also reported, showing how the phase transition occurs and listing which properties are system-dependent. Finally, a general outline of the goals of the thesis and its general organization are reported.

## 1.1   A War Technological Problem

The history[1] of BaTiO$_3$ is tightly linked to the micas, imported from South America, a dielectric phyllosilicate commonly employed in capacitors for military purposes, back in the '40s. With the advent of WWII and the threaten of German U-boats to sink the suppliers' boats, the United States government decided to invest in the research for an alternative solution. That brought to the discovery and employment of the BaTiO$_3$ (BTO) ceramics in spite of micas. The discovery of BTO were performed between the 1941 till 1944 in USA, Russia and Japan, respectively. The first patent describing the process of synthesis of BTO was deposited by Thurnaarer and Deaderick[2] from the American Lava Company in 1941, U.S. Patent No. 2.429.588. It has been speculated that German scientists delayed the discovery of BTO because of the extraction process of TiO$_2$: the methods based on chloride exploited by USA, Russia and Japan led to a lower content of niobium (Nb), therefore a lower conduction was detected with respect to the extracted material via sulfuric acid route used in Germany. In 1945 and 1946, von Hippel[3] (USA) and Wul and Goldman[4] (Russia), independently demonstrated the ferroelectric switching in BTO ceramics. In fact, ferroelectricity[1] was believed to be a property only present in potassium dihydrogen phosphate (KH$_2$PO$_4$) and related crystals, as a consequence of an order-disorder phase transition.

## 1.2   The BaTiO$_3$ Compound

The discovery of ferroelectricity and piezoelectricity[2] in polycrystalline BaTiO$_3$ ceramics prompted to a cascade of independent researches on this topic right after the end of WWII. The potential use of these new compounds could be extended to sensors, transducers and actuators. Major scientific advances were reported by Megaw[5], Kay and Vousden[6] in UK, and Miyake and Ueda[7] in Japan, which were able to understand first, and rationalize after, the structure and phase crystal changes through cooling process. Later in 1947, Blättner and coworkers were able to synthesize the first BTO single crystal in Switzerland via ternary melts. Because the procedure to obtain high-quality single crystals was quite expensive, the discovery of the poling process for BTO ceramic powder marked another breakthrough. In fact, the polarization of a system was though to occur only in single-crystal systems, and the possibility to re-orient it was not yet known. This discovery[8] allowed to implement polycrystalline ceramics for piezoelectric applications, displaying an improved mechanical robustness and a lower manufacturing cost. In the following years, between 1947 and 1950, the first commercial technologies based on BaTiO$_3$ polycrystalline system were put in productions, *i.e.*, by-pass capacitors, accelerometers, transducers for ultrasonic generation, phonograph pickups and capacitors. The peculiar nature of BTO system is also at the origin of the Devonshire[9, 10] theory[3], which aims at phenomenologically reconcile its phase transition, dielectric, electromechanical and thermal properties. The decade that followed the discovery of ferroelectric ceramics was characterized by a incredibile effort to explore new solid

---

[1]   **Definition**: "Property of certain non-conducting crystalline systems, or dielectrics, which exhibits polarization, *i.e.*, separation of the center of positive and negative electric charges, making one side of the crystal positive, the other negative. This process can be reversed in direction by applying an external electric field."

[2]   **Definition**: "Property of certain non-conducting crystals that display negative and positive charge separation on opposite sides due to mechanical pressure or stress. Piezoelectricity is displayed by 20 out of 32 crystal classes."

[3]   The Devonshire theory can be classified as part of the statistical thermodynamics theories for explaining phase transition as reported by Ginzburg[11], Landau and Lifshitz[12].

solutions that could enhance the already unique properties of BTO. An example of this "*gold rush*" is the explorative synthesis of quaternary solid-state solutions by McQuarrie and Behnke[13] between BaTiO$_3$, BaZrO$_3$, CaZrO$_3$ and CaTiO$_3$ and Coffeen[14] between BaTiO$_3$, BaSnO$_3$, CaSnO$_3$ and SrSnO$_3$. The exploration of potential polycrystalline ceramics displaying remarkable ferroelectric and piezoelectric properties, started during WWII, is still ongoing in the current days. In fact, despite the effort, this class of compounds still suffers from a limited temperature range of operability when acting as piezoelectrics[15].

The BaTiO$_3$ compound, whose general formula ABO$_3$ is a clear reference to perovskite class of systems, displays the Ba$^{2+}$ - A-site - at the corners of the cubic unit cell, while the Ti$^{4+}$ is located on the B-site of the cell center. The O$^{2-}$ anions instead are located on the face centers of the cubic cell, where they form the BO$_6$ octahedra. When cooled at ambient pressure, the BaTiO$_3$ undergoes to first-order phase transition, as schematically reported in fig. 1.1, going from cubic crystalline habit ($Pm\bar{3}m$) $\xrightarrow{\sim 131°C}$ tetragonal ($P4mm$) $\xrightarrow{\sim 0°C}$ orthorombic ($Amm2$) $\xrightarrow{\sim -90°C}$ rhombohedral ($R3m$). The spontaneous polarization of BaTiO$_3$
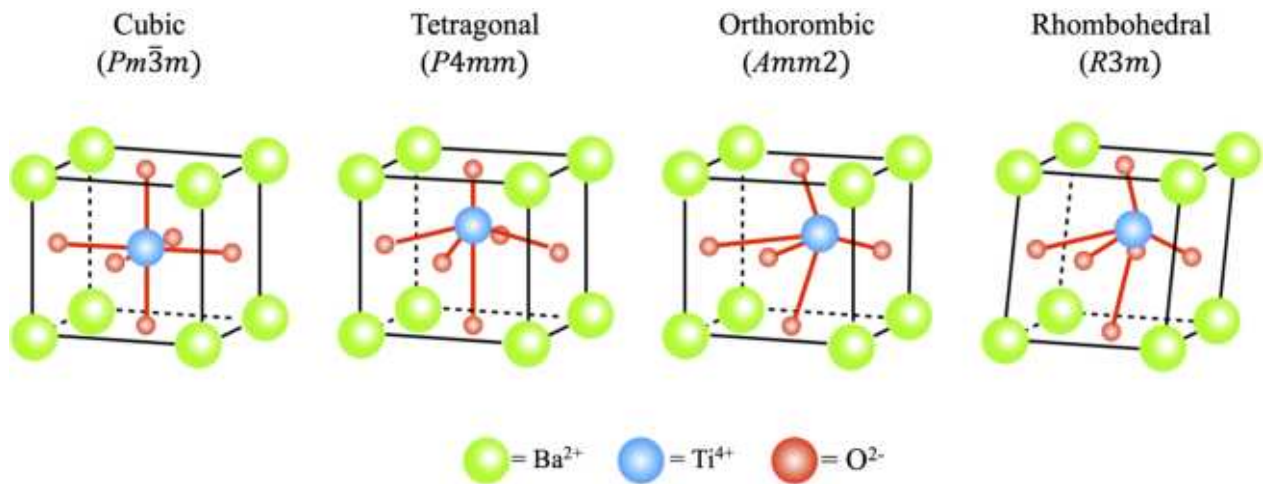


**Figure 1.1:** Schematic representation of the phase transition in BaTiO$_3$ system during the cooling process at ambient pressure. Each structure is associate with its crystalline space group habit.

is usually related to the structural shift that both Ti$^{4+}$ and O$^{2-}$ undergo during phase transition, from cubic to tetragonal. Above 131°C, the Curie temperature for BTO, the dielectric susceptibility follows the Curie-Weiss[4] law, meanwhile below $T_C$, the re-orientation of the polarization direction happens, sometimes referred as *inter*-ferroelectric transition.

---

[4] The Curie-Weiss law for the dielectric susceptibility $\eta$ is

$$\eta \approx \frac{\varepsilon'}{\varepsilon_0} = \frac{C}{T - T_C}$$

where C is the Curie constant, $T_C$ is the Curie-Weiss temperature, $\varepsilon'$ is the real part of the dielectric permittivity and $\varepsilon_0$ is the permittivity of the free-space. Below $T_C$, the system displays spontaneous magnetization.

**Doping BaTiO₃**

The thesis aims at being an explorative *ab-initio* computational work for assessing the quality of two different computational methodologies, based on plane-waves and Gaussian-type orbitals, respectively, for studying solid-state systems in general, by testing $BaTiO_3$ in particular. The study will go through three main steps:

- Step 1: comparison of the optimized unit cell parameters, bond lengths between atomic species and related electronic structure properties, *i.e.*, Density of States (DOS) and Band structure, as obtained from the two computational methodologies employed.

- Step 2: comparison of cell parameters, bond lengths between atomic species and electronic structure (DOS and band structures) of the doped BTO supercell with strontium (Sr) and tin (Sn) at 25%, exploiting the supercell approach.

- Step 3: comparison of cell parameters, bond lengths between atomic species and electronic structure (DOS and band structures) of the doped BTO supercell with strontium (Sr) and tin (Sn) at 50%, exploiting the supercell approach.

# 1.3 Thesis Goal and Outlook

The use of plane wave and all-electron basis set for the same purposed can help outline similarities and differences between the two approaches by exploring and investigating the complex nature of $BaTiO_3$ perovskite-like system. The thesis is organized as follows:

- **Chapter2**: the general description of the computational framework is introduced, with particular emphasis on the Density Functional Theory approach. The general description of the plane wave and all-electron basis set, together with the general description of the atomic species via pseudopotentials and/or Gaussian type orbitals are briefly introduced. This chapter ends with a description of the key properties that are investigated and reported.

- **Chapter3**: to assess the quality of the methodologies to employ in the study of the BTO system, sometimes before data production, a quality check of the pseudopotentials to use and some key parameters is required. This is particularly true in case of the plane waves codes. As such, in this chapter the quality check of the key parameters for the plane wave code will be presented. Moreover, a comparative study of the $BaTiO_3$ unit cell, space group $Pm\bar{3}m$, will be reported between plane waves and all-electron basis set, at the same level of theory. The chapter ends with a comparison of the basis properties of the system, *i.e.*, density of states (DOS), band structure and possibile, bulk modulus.

- **Chapter4**: the study of a series of doped $BaTiO_3$ supercells, with a strontium (Sr) atom replacing a barium (Ba) one (Sr→Ba) and a tin (Sn) atom replacing a titanium (Ti) one (Sn→Ti), is reported. The doping in both cases is performed at 25% and 50%, following the supercell approach, and structural and electronic properties explored with both plane waves and gaussian basis set, respectively.

- **Chapter5**: the conclusion of the thesis are drawn and the outline for future work in the study of the $BaTiO_3$-based systems with perovskite-like structure is provided.

# Chapter 2

# Methodology

In this chapter, the computational framework put in place to study the properties of the barium titanate compound is presented. A brief introduction is devoted to the Density Functional Theory (DFT) methodology, which plays a relevant is the role in this work. It will follow the explanation of its implementation in both the plane waves and all-electron configuration, and the general description of the properties (Band Structure, Density of States, etc.) calculated via DFT.

# 2.1 Density Functional Theory

The key advantage of the Density Functional Theory (DFT) methodology is the good compromise it offers between accuracy and computational cost. Moderately large systems can be easily investigated, allowing to elucidate the electronic structure of the atoms, molecules, and solids. The DFT methodology is based on functionals, *i.e.*, a mapping of an entire function $f$ to a resulting number $F[f]$; whereas a common function is defined to be a mapping of a variable $x$ to a number $f(\mathrm{x})$. DFT allows to describe the electronic structure of atoms, molecules, and solids throughout the 3D electronic density $\rho$, upon which functionals depend. The groundbreaking article published by Hohenberg and Kohn[16] in 1964 led to the practical development of the DFT approach, showing that a functional $F[f]$ exists such that the ground state energy can be expressed as the minimum of the functional:

$$E[\rho] = F[\rho] \int d\mathbf{r} \ V(\mathbf{r})\rho(\mathbf{r}) \tag{2.1}$$

where $\rho(\mathbf{r})$ is the charge density, and $F[\rho]$ does not depend on the system. It follows that the ground state properties of the system of interacting electrons can be described in terms of the charge density only, rather than on the far more complicated many-particle wave function.

**Thomas-Fermi Model**

The original DFT method developed by Thomas and Fermi[17, 18] in 1927 reported the kinetic energy of the system of electrons to be approximated by an energy functional of the density. In this system under consideration, electrons do not interact to each other but they belong to a homogeneous gas displaying a density that is equal to the local density at any given point. The kinetic energy functional proposed by Thomas and Fermi is:

$$T_{TF}[\rho] = \frac{3}{10}(3\pi^2)^{\frac{2}{3}} \int \rho(\mathbf{r})^{\frac{5}{3}} d\mathbf{r} \tag{2.2}$$

It follows that the energy of an atom can be estimated using the functional

$$E_{TF}[\rho(\mathbf{r})] = \frac{3}{10}(3\pi^2)^{\frac{2}{3}} \int \rho(\mathbf{r})^{\frac{5}{3}} d\mathbf{r} - Z \int \frac{\rho(\mathbf{r})}{\mathbf{r}} d\mathbf{r} + \frac{1}{2} \int \frac{\rho(\mathbf{r_1})\rho(\mathbf{r_2})}{\mathbf{r_{12}}} d\mathbf{r_1} d\mathbf{r_2} \tag{2.3}$$

where $Z$ is the nuclear charge in atomic units. The correct density to be used in 2.3 is estimated by means of the variational principle, by minimizing the functional for all possible $\rho(\mathbf{r})$, under the constraint on the total number of electrons

$$\int \rho(\mathbf{r}) d\mathbf{r} = N \tag{2.4}$$

**Variational Principle**

The variational principle applied to the density function $\rho(\mathbf{r})$ states that

> *the energy computed from a guessed density function $\rho(\mathbf{r})$ is an upper bound to the true ground state energy $E_0$*

from which it follows that the full minimization of the functional $E[\rho]$ *w.r.t.* all allowed $N$-electrons wavefunctions will give the true ground-state, $\rho_0$, and the corresponding energy, $E_0$. The variational principle provides a way to determine the ground-state wavefunction $\psi_0$ and energy $E_0$ for a given system of $N$ electrons and a given nuclear potential $V_{ext}$, that is

$$E_0 = E[N, V_{ext}] \tag{2.5}$$

## 2.1.1 The Kohn-Sham Method

The revolutionary idea that made DFT viable in practical terms was proposed by Kohn and Sham[19] in 1965. The idea was to replace the many-body Hamiltonian[1]

$$\hat{H} = \hat{T}_N + \hat{T}_e + \hat{V}_{NN} + \hat{V}_{ee} + \hat{V}_{Ne} \tag{2.6}$$

where

- $\hat{T}_N$ is the nuclear kinetic energy

- $\hat{T}_e$ is the electronic kinetic energy

- $\hat{V}_{NN}$ is the internuclear repulsion potential energy operator

- $\hat{V}_{ee}$ is the interelectronic repulsion potential operator

- $\hat{V}_{Ne}$ is the electron-nuclei attraction potential energy operator

with an *auxiliary* system, form by a set of independent and non-interacting particles. The so-called Kohn-Sham (KS) *ansatz* assumes that the ground-state density of the original interacting system is equal to that of the non-interacting one. This *ansatz* is based on two key assumptions:

1. The exact ground-state density is equal to the ground-state density of the auxiliary system of non-interacting particles

2. The auxiliary Hamiltonian is chosen in order to have the usual kinetic operator and an effective local potential $V_{\text{eff}}^{\sigma}(\mathbf{r})$ acting on an electron of spin $\sigma$ at point $\mathbf{r}$. The local form is not essential, but it is a useful simplification which is considered as one of the KS equation main features.

The KS *ansatz* can be graphically summarized as
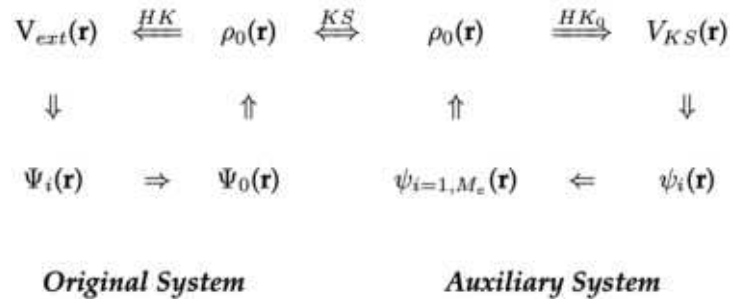


**Figure 2.1:** Schematic representation of the KS ansatz linking the original many-body system to the auxiliary one.

---

[1] The analytic expression form of the Hamiltonian in 2.6 is

$$\hat{H} = -\frac{1}{2} \sum_{A=1}^{M} \frac{\nabla_A^2}{M_A} - \frac{1}{2} \sum_{i=1}^{n} \nabla_i^2 + \sum_{A=1}^{M} \sum_{B>A}^{M} \frac{Z_A Z_B}{r_{AB}} + \sum_{i=1}^{n} \sum_{j>i}^{n} \frac{1}{r_{ij}} - \sum_{i=1}^{n} \sum_{A=1}^{M} \frac{Z_A}{r_{iA}}$$

where $i$, $j$ and $A$, $B$ refer to electrons and nuclei, respectively; $M_A$ and $Z_A$ denote the mass and nuclear charge of nucleus $A$, $r_{iA}$ is the distance between electron $i$ and nucleus $A$, $r_{ij}$ is the distance between electron $i$ and electron $j$, and $r_{AB}$ is the distance between nucleus $A$ and nucleus $B$.

---

## 2.1.2   The Kohn-Sham Equations

The key question is to understand how the fundamental physical quantities of the real system are accounted in the DFT method. To do so, it is important to reconsider the KS *ansatz*: "the ground-state density of the interacting system is considered to be equal to the ground-state of the non-interacting one". The electron density $\rho(\mathbf{r})$ and the kinetic energy $T_{\mathrm{KS}}[\rho]$ can be defined as

$$\rho(\mathbf{r}) = \sum_{i=1}^{N} |\psi_i(\mathbf{r})|^2 \tag{2.7}$$

and

$$T_{\mathrm{KS}}[\rho] = -\frac{1}{2} \sum_{i=1}^{N} \langle \psi_i | \nabla^2 | \psi_i \rangle \tag{2.8}$$

where $\psi_i$ represents the occupied molecular orbitals and the sum runs over each occupied molecular orbital $N$. In a similar way, the kinetic energy of the complex system is replaced by the kinetic energy from the auxiliary one, so that a universal functional $F[\rho]$ can be written as

$$F[\rho] = T_{\mathrm{KS}}[\rho] + E_{\mathrm{HT}}[\rho(\mathbf{r})] + E_{\mathrm{xc}}[\rho] \tag{2.9}$$

In this expression, the $T_{\mathrm{KS}}[\rho]$ term represents the kinetic energy functional of the auxiliary system which depends upon the electronic ground-state density $\rho_0$, while the second term represents the Hartree energy in terms of the Hartree density and potential as

$$E_{\mathrm{HT}}[\rho(\mathbf{r})] = \frac{1}{2} \int \frac{\rho(\mathbf{r}) n(\mathbf{r}')}{|(\mathbf{r}) - (\mathbf{r}')|} d(\mathbf{r}) d(\mathbf{r}') \tag{2.10}$$

The complex many-body effects due to exchange and correlation are then condensed in the exchange-correlation energy term $E_{\mathrm{xc}}[\rho]$, which can be written in terms of the HK functional as

$$E_{\mathrm{xc}}[\rho] = F_{\mathrm{HK}}[\rho] - (T_{\mathrm{KS}}[\rho] + E_{\mathrm{HT}}[\rho]) \tag{2.11}$$

In this respect, the determination of the orbitals $\psi_i$ proceed in a similar way like in the Hartree-Fock method, but solving this time the so-called KS-equations

$$H^{\mathrm{KS}} \psi_i^{\mathrm{KS}} = \epsilon^{\mathrm{KS}} \psi_i^{\mathrm{KS}} \quad \text{for} \quad i = 1, ..., N \tag{2.12}$$

where the $H^{\mathrm{KS}}$ is the KS operator. In KS-DFT, differently from the Hartree-Fock theory, where only exchange but not correlation is included, the exchange-correlation potential operator $\mathrm{V}_{\mathrm{xc}}(\mathbf{r})$ groups all the many-body effects in one term. The optimization of the orbitals $\psi_i$ is performed self-consistently, leading at convergence to the ground-state density of the system investigated. *Apriori*, the obtained optimized density can lead to obtain all the remaining properties of the system considered. Nonetheless, it is not known what exact form the exchange-correlation potential term should have, which lead, along the years, to a plethora of exchange-correlation functionals trying to approximate it. Among the most widely used it is worth mentioning the Local Density Approximation (LDA), Generalized Gradient Approximation (GGA) and the hybrid ones, like B3LYP.

**Local Density Approximation**

The Local Density Approximation (LDA), which considers the exchange-correlation potential term of a given particle locate in $\mathbf{r}$, depends on the the electronc density $\rho$ at a specific point, specifically

$$E_{\text{xc}}^{\text{LDA}} = \int \rho(\mathbf{r})\epsilon_{\text{xc}}^{\text{LDA}}[\rho(\mathbf{r})]d\mathbf{r} \tag{2.13}$$

where the $\epsilon_{\text{xc}}^{\text{LDA}}$ term represents the sum of the exchange and correlation quantities

$$\epsilon_{\text{xc}}^{\text{LDA}}(\mathbf{r}) = \epsilon_{\text{x}}^{\text{LDA}}(\mathbf{r}) + \epsilon_{\text{c}}^{\text{LDA}}(\mathbf{r}) \tag{2.14}$$

Specifically, while the exchange terms is derived from the uniform electron gas definition for a fix point $\mathbf{r}$ as

$$\epsilon_{\text{x}}^{\text{LDA}}(\mathbf{r}) = -\frac{3}{4}\left(\frac{3}{\pi}\right)^{\frac{1}{3}}\rho(\mathbf{r})^{\frac{4}{3}} \tag{2.15}$$

menawhile the correlation terms are inferred from parametric equations fitting perturbative or Quantum Monte Carlo[20, 21] results. The most used are the Wigner[22], Perdew and Wang[23, 24] (PW92), Lee-Yang-Parr[25], Perdew-Zunger[26] (PZ). The LDA, being exact for the uniform electron gas, is well suited for the investigation of homogeneous densities (*e.g.*, systems based on elements of the $s$ and $p$ block.) However, for systems displaying inhomogeneous densities, it is necessary to also account for the shape of $\rho(\mathbf{r})$ around point $\mathbf{r}$, that is, the density gradient.

**Generalized Gradient Approximation**

The Generalized Gradient Approximation (GGA) differs from the LDA one for containing the gradient of the functional as extra term, introducing a semi-local character of the electron density in the definition of $E_{\text{xc}}$. This allows to account for the shape that $\rho(\mathbf{r})$ assumes around point $(\mathbf{r})$

$$E_{\text{xc}}^{\text{GGA}}[\rho, \nabla\rho] = \int \rho(\mathbf{r})\epsilon_{\text{xc}}^{\text{GGA}}(\rho(\mathbf{r}), \nabla\rho(\mathbf{r}))d\mathbf{r} \tag{2.16}$$

Thus, the exchange energy terms become

$$E_{\text{xc}}^{\text{GGA}}[\rho, \nabla\rho] = \int F_{\text{x}}\ s(\mathbf{r})\rho(\mathbf{r})^{\frac{4}{3}}d\mathbf{r} \tag{2.17}$$

with $F_{\text{x}}$ being the reduced density gradient

$$s(\mathbf{r}) = \frac{|\nabla\rho(\mathbf{r})|}{6\pi^2\rho(\mathbf{r})^{\frac{4}{3}}} \tag{2.18}$$

In this sense, a great effort was placed and is still put in developing suitable GGA functionals because of their ability to provide a consistent and reliable description for the system not only based on the elements of the $s$ and $p$ block, but also to some extent to the $f$ and $d$ block ones. Among the most popular GGA functionals, the there is the PBE[27, 28] one, also used in this work for the structural optimization reported.

**Hybrid Functionals**

Another class of popular functionals that displayed great success in terms of properties, both structural and electronic ones, are the hybrid functionals. These functionals, introduced by Becke in 1993, account for a part of "*exact exchange*" derived from the Hartree-Fock exchange and a part inferred by interpolation of post-Hartree-Fock and semi-empirical results. A popular hybrid functional is the B3LYP[28, 29] one, which stands for Becke, 3-parameters, Lee-Yang-Parr, and defined as

$$E_{xc}^{B3LYP} = (1 - a_0)E_x^{LDA} + a_0 E_x^{HF} + a_x \Delta E_x^{B88} + a_c E_c^{LYP} + (1 - a_c)E_c^{VWN} \tag{2.19}$$

where $a_0 = 0.20$, $a_x = 0.72$ and $a_c = 0.81$. The $E_x^{LDA}$ is the standard local exchange functional[30], $\Delta E_x^{B88}$ is Becke's gradient correction to the exchange functional, $E_c^{LYP}$ is the term for the correlation functional from Lee, Yang and Parr[25], and finally, $E_c^{VWN}$ is the Vosko-Wilk-Nusair[31] local density approximation to the correlation functional.

### 2.1.3 Kohn-Sham in Plane Waves Basis-Set

The nature of crystalline systems inspired the development of DFT theory based on plane waves, suitable to reproduce the repetitive network of atomic and molecular units. The Bloch theorem[32] is efficiently exploited to express the one-electron wavefunction in terms of Fourier expansion; moreover, plane waves is a mathematical tools relatively simple to handle, which has the advantage to cover the space equally. This is particularly important if, *a priori*, the form of the wavefunction is unknown. To achieve a finite basis set, the Fourier expansion of the plane wave must be truncated. This is done by introducing a kinetic energy cutoff $E_{cut}$ as

$$E_{cut} = \frac{\hbar^2}{2m}|\mathbf{k} + \mathbf{G}|^2 \tag{2.20}$$

where $\mathbf{k}$ is the wave vector and $\mathbf{G}$ is the reciprocal lattice vector. The choice of $E_{cut}$ determines the truncation of the plane waves expansion at a particular $\mathbf{G}$. The KS equations can be reformulated as

$$\sum_{G'} \left[ \frac{1}{2}|\mathbf{k} + \mathbf{G}|^2 + V_{ion}(\mathbf{G} - \mathbf{G}') + V_H(\mathbf{G} - \mathbf{G}') \right] c_{i,\mathbf{k}+\mathbf{G}} = \epsilon_i c_{i,\mathbf{k}+\mathbf{G}} \tag{2.21}$$

where the reciprocal space of the kinetic energy is diagonal and the potentials are described in terms of Fourier components. This secular equation can be solved by diagonalizing the Hamiltonian matrix $H_{\mathbf{k}+\mathbf{G},\mathbf{k}+\mathbf{G}'}$. As such, the size of the matrix is defined by the energy cutoff $E_{cut}$. The final energy value depends upon the pseudopotential employed to describe the atomic species composing the molecule or crystal.

**Pseudopotentials**

In general, if both core- and valence electrons of each atomic species are accounted, the plane waves expansion computational cost would quickly become prohibitive. Besides, because of the *different* nature of the two kinds of electrons, higher $E_{cut}$ values would be required: the core ones strongly bound to the nucleus, the valence ones highly flexible. Because the majority of the physical properties are consequence of the interactions of the valence electrons of neighboring atoms, then it comes in handy to separate the core- from the valence-contributions, respectively.
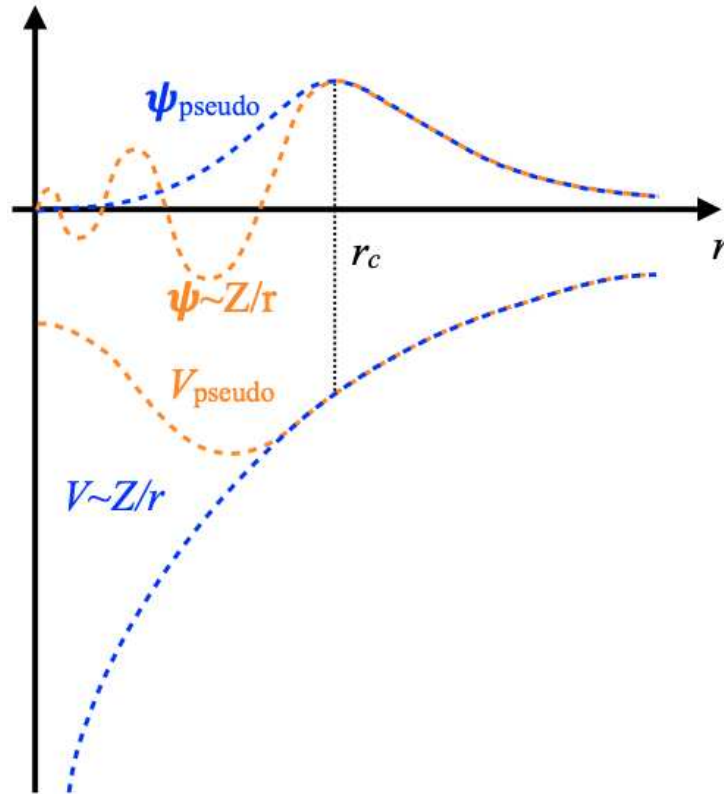
**Figure 2.2:** Scheme showing the trend of a pseudo wavefunction and potential (orange), compared to the real Coulomb potential and wavefunction trend of a nucleus (blue). The match between real and pseudo wavefunction is found above a certain cutoff radius $r_c$

The pseudopotential is a mathematical approximation of the effective potential that mimics the effect of ionic nuclei and core electrons, see fig. 2.2. As such, the core states are frozen and not explicitly taken into consideration, meanwhile the valence electrons are described by means of pseudo wavefunctions, which makes plane waves DFT practicable. Two key properties are pivotal in the pseudopotential generation: *a*) smoothness, *i.e.*, a pseudopotential should be as smooth as possibile to have a convenient plane waves expansion, thus small $E_{cut}$; *b*) transferability, *i.e.*, accuracy, related to the ability of the pseudopotential to generate pseudo-orbitals that are as much accurate as possible to the true orbitals outside the core region, for all the system containing a given atom[32]. Pseudopotentials come in different *flavors*, among which the most popular ones are the ones called Norm-Conserving[33] (NC) and Ultrasoft[34] (US):

- Norm-Conserving Pseudopotentials (NC): this class of pseudopotentials are generated following a specific set of requirements, as defined by Hamann, Schlüter and Chiang[33], that guarantee both transferability and smoothness, fixing that:

  1. the pseudo-valence and all-electron eigenvalues coincide for a chosen prototype atomic configuration.

  2. The all-electron and pseudo atomic wave functions coincide beyond a chosen core radius $r_c$[32]. **Consequence**: the potential is uniquely determined by the wavefunction and energy $\epsilon$.

3. The logarithmic derivates of the all-electron and pseudo-wave functions coincide in $r_c$. **Consequence**: it follows that both the wavefunction $\psi_i$ and its first derivative $W_{ln}$, defined as

$$
W_{ln}(\epsilon, r) = r \frac{\psi_i'(\epsilon, r)}{\psi_i(\epsilon, r)} = r \frac{d}{dr} ln \ \psi_l(\epsilon, r)
$$

are continuous in $r_c$ for any smooth potential.

4. The charge, integrated inside $r_c$, agrees for each wavefunction. **Consequence**: the integrated charge

$$
Q_{ln} = \int_0^{R_c} dr \ r^2 |\psi_{ln}(r)|^2 = \int_0^{R_c} dr \ \phi_{ln}(r)^2
$$

is the same for $\Psi_l^{PS}$, radial pseudo-potential, as for the all-electron radial orbital $\psi_l^{PS}$, for a valence state. $Q_{ln}$ conservation ensure that $i$) the total charge in the core region is correct and $ii$) the normalized pseudo-potential is equal to the orbital outside $r_c$. In other words, this constraint on the charge ensures that the wavefunction $\psi_l(r)$ and its radial derivative $\psi_l'(r)$ are continuous at $r_c$, for any smooth potential, leading to the correct representation of the region between atoms, *i.e.*, outside $r_c$.

5. The first energy derivative of the logarithmic derivates of both the all-electron and pseudo-wave functions coincides in $r_c$. **Consequence**: pseudopotentials are guaranteed to adapt as a function of the system to simulate.

• Ultrasoft Pseudopotentials (US): this class of pseudopotentials, introduced by Vanderbilt[34] in 1990, relaxes the NC conditions listed above to generate softer potentials, which in turn require a smaller amount of plane waves. Nonetheless, these relaxed conditions are related to some loss of transferability. The pseudo-wavefunctions are allowed to be as much soft as possibile within the core region, leading to a dramatic reduction of the kinetic $E_{\text{cut}}$ values. From a technical perspective, this is achieved by introducing a generalized orthonormality condition. The electron density $\rho(\mathbf{r})$, see eq. (2.7), has to be augmented in the core region to recover the full electronic charge. $\rho(\mathbf{r})$ is then subdivided in two contributions:

  – a hard part located in the core region;

  – a smooth part that extends in the unit cell.

The augmented contribution appears only in the density, but not in the wavefunctions. Another advantage that comes with the US generation is done by the algorithm used to generate them, which guarantees good scattering properties over a pre-specified energy range, resulting in a much better transferability and accuracy of pseudopotentials. US usually also treats "shallow" core states as valence by including multiple sets of occupied states in each angular momentum channel. This also contributes to high accuracy and transferability of the potentials, although at a price of computational efficiency.

## 2.1.4   All-Electron Basis-Set

The study of molecular and solid-state systems at DFT level can also be pursued by means of a different set of mathematical functions describing the atomic orbitals[35]. This alternative basis is composed by a set of mathematical functions describing the atomic orbitals of each atomic species centered at each atomic position. The resulting molecular orbital $\psi_i$ is then represented by a Linear Combination of Atomic Orbitals[36] ($\phi_i$) (LCAO). These atomic orbitals are generally known to display an exponential decay with the distance $r$ from the nucleus of the atom of the following form

$$\phi_i \propto e^{-r} \tag{2.22}$$

Their linear combination generates a molecular orbital $\psi_i$ as

$$\psi_i = \sum_m a_m \phi_m \tag{2.23}$$

where the $a_m$ coefficients "weight" the different contributions to form the electronic structure of the atomic species. The resulting molecular orbitals are iteratively optimized till convergence is reached optimizing the $a_m$ coefficients.

**Slater Type Orbitals** *vs.* **Gaussian Type Orbitals**

The physically motivated type of orbitals that better reproduces the correct trend far away from the nucleus are the Slater-type of orbitals[37] (STO), introduced by John C. Slater back in the 1930. Unfortunately, the use of the STO atomic orbitals displays a relevant disadvantage: their mathematical employment makes quite a challenge the solution of the interactions terms for exchange and correlation. An alternative to the use of STO basis set was proposed by Boys in 1950, replacing the complex Slater-type orbitals, proportional to $e^{-r}$, with a Gaussian-type of orbitals[38] (GTO), proportional to $e^{-r^2}$, see fig. 2.3. GTO mathematically display the advantage of being more easily tractable but the disadvantage of only partially capturing the correct asymptotic decay trend of the STO. However, the
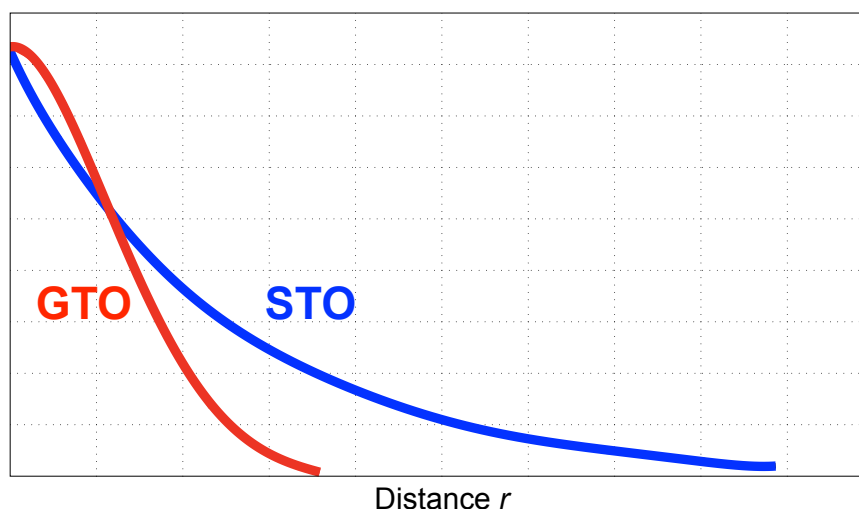


**Figure 2.3:** Graphical representation of the Slater-type Orbitals (STO) in red and Gaussian-type Orbital (GTO) in blue.

use of a single GTO is not sufficiently accurate to replace a single STO; it follows that a linear combination of GTO, can then be employed in these terms, using *de facto* the GTO as basis functions

$$\phi_h = \text{STO} \approx \sum_h c_h(\text{GTO})_h \quad \text{where} \quad (\text{GTO})_h \propto e^{-\alpha_h \cdot r^2} \tag{2.24}$$

The $\phi_h$ term represents the resulting orbital from LCAO, in analogy to eq. (2.22), while the $c_h$ terms represent the coefficients of the linear combination, while the $\alpha_h$ ones represent the coefficients determining the evolution of each gaussian function, respectively. Each single GTO is referenced as *primitive*, and a basis set generated starting from a linear combination of GTO is called *contracted*. In general, increasing the number of primitives leads to better approximated atomic orbitals, but also to a rapid increase of the computational cost. Following this logic, one of the first GTO basis set to be developed and used was the so-called STO-3G: that is, each Slater-type orbital (STO) is approximated by a linear combination of three Gaussian primitive functions $\phi_h$. The resulting molecular orbitals $\psi_i$ are found by the subsequent optimization (throughout the iterative process) of the coefficients of the atomic orbitals approximated by the primitive GTO basis functions

$$\psi_i = \sum_m a_m \phi_m = \sum_m a_m \sum_h c_h(\text{GTO})_h \tag{2.25}$$

where only the $a_m$ coefficients are optimized, while the $c_h$ ones are kept fixed. The STO-3G basis set represents a class of basis set called single-$\zeta$ (=single-zeta), which "*treats*" both the core and valence electrons in the same way. It has been noticed that, despite increasing the number of basis functions, *e.g.*, moving from STO-3G to STO-5G, while the accuracy does not increase substantially, the computational cost does. Considering that the majority of the molecular and material properties come from the valence electrons interactions, a new class of basis set called multiple-$\zeta$ was proposed, specifically called *split-valence* basis set. One of the earlier examples of this class of basis set is, for instance, the 3-21G basis set, that is, the core orbitals are approximated by a single-$\zeta$ basis set, *i.e.*, one contraction of 3 primitive Gaussians functions is used for each core orbital ; meanwhile, valence orbitals are double-$\zeta$, *i.e.*, each valence orbital is approximated by a contraction of 2 Gaussian functions plus 1 extra, providing more flexibility. Subsequently, the computational cost increases, but there is a certain gain in terms of accuracy. In the last three decades a plethora of multiple-$\zeta$ basis sets have been reported, sometimes tailoring them to specific sets of compounds or properties. In case of periodic systems, the same kind of basis set can be employed in order to obtain the crystalline orbitals, this time employing, like in the plane waves framework, the Bloch theorem. Sometimes, basis set employed to describe atomic species displaying large atomic numbers are approximated by effective core potentials[39] (ECP). These ECP, similar to the pseudopotential concept used in plane waves basis set, approximate the core part of the atom by replacing it with an effective potential, eliminating a large portion of basis function that are otherwise required to properly simulate the system considered, and consequently reducing the computational cost.

## 2.1.5 Properties Investigated

**Band Structure**

The reciprocal basic unit of repetition belonging to a periodic systems is called Brillouin zone (BZ). The elements of symmetry that are characteristic of the BZ represent the irreducible part (IBZ), whose characteristic vectors are usually referred as $\vec{k}$. To obtain the density and total energy, it is necessary to solve continuous integrals at, in principle, an infinite number of $\vec{k}$-points. Nonetheless, to solve the resulting integrals, the discretization of the $\vec{k}$-space to only few $\vec{k}$-points is necessary, rewriting the integrals as a weighted sum

$$\sum_n \int_{\text{BZ}} d^3k F(\mathbf{k}) \approx \sum_{\mathbf{k}} [\omega(\mathbf{k}) \cdot F(\mathbf{k})] \tag{2.26}$$

where $\omega(\mathbf{k})$ are the weights containing the effects of symmetry that must sum up to 1, and $F(\mathbf{k})$ is a lattice periodic function. The resolution of this expression is related to the sampling of the BZ for a small number of $\vec{k}$-points, finding their integration weights, and resolving the DFT equations at these selected $\vec{k}$-points. Generally, the simpler manner to achieve this is by using an even-space integration grid of $\vec{k}$-points along the directions of the reciprocal lattice vectors. In general, the $\vec{k}$-points mesh, depending on the system considered, needs to be tested, in order to achieve the best compromised between computational cost and accuracy. As mentioned above, periodic systems allows to effectively exploit the Bloch theorem. In this sense, the eigenfunction of the one-electron Hamiltonian can be expressed as

$$\phi(\mathbf{x}) = \sum_{\mathbf{k}} A_{\mathbf{k}} \phi_{\mathbf{k}}(\mathbf{k}) = \sum_{\mathbf{k}} A_{\mathbf{k}} e^{i\mathbf{k}\mathbf{x}} u_{\mathbf{k}}(\mathbf{x}) \tag{2.27}$$

where $A_{\mathbf{k}}$ are constants. The one-electron wavefunctions can be labelled by a constant $\mathbf{k}$, which represents the wave vector in the Bloch functions. The energy plot *vs.* $\mathbf{k}$ that is subsequently derived is known as band structure. Alternatively, band structure path of a specific system can also be defined exploiting Group Theory (GT). The approach of the GT is only here briefly discussed. Group Theory is a mathematical branch that studies the so called Groups, where a group is an algebraic structure characterized by an associative binary operation, equipped with a neutral element, for which every element belonging to the structure owns an invert element. Various physical systems, such as crystals and the hydrogen atom, can be modeled by symmetry groups. Band structure diagrams are like maps and the group theory notations are like symbols on the map. Understanding symbols means exploring the electronic properties of the material under investigation. Special high symmetry points in the BZ are labelled as, *e.g.*, $\Gamma$, $\Delta$, etc., according to the unit cell symmetry in the reciprocal space. Energy bands allows to explore and classify the nature of the gaps in crystalline solids, namely

- *indirect band gap*: the closest states found right above and below the band gap that do not share the same $\mathbf{k}$ vector;

- *direct band gap*: the closest states found right above and below the band gap that share the same $\mathbf{k}$ vector.

### Density of States

The density of states (DOS) of a system describes the number of energetic states that are available to the electrons. The DOS at a certain energy level E is equal to the sum of the energy levels between E and E+$d$E with respect to the energy interval $d$E

$$\text{DOS}(E) = \frac{1}{N_{\mathbf{k}}} \sum_{i,\mathbf{k}} \delta(\epsilon_{i,\mathbf{k}} - E) \tag{2.28}$$

while the DOS per unit of volume $\Omega$ in extended systems is

$$\text{DOS}(E) = \frac{\Omega}{(2\pi)^d} \int_{\text{BZ}} d\mathbf{k} \ \delta(\epsilon_{i,\mathbf{k}} - E) \tag{2.29}$$

In the independent-particles states, the equations above represent the number of independent particles states per unit of energy, where $\epsilon_{i,\mathbf{k}}$ represents the energy of an electron. The DOS can be obtained once the orbitals of the system are known, allowing to discern the nature of the material under investigation, *i.e.*, insulator, conductor or semi-conductor.

### Equation of State

The equation of state (EOS) is an equation that relates pressure, volume and bulk modulus of a body. There are several EOS, but the one used in this work is the so-called Birch-Murnaghan[40, 41], proposed by Birch in 1947 and based on the work of Murnaghan from the 1944. It is a third order isothermal equations defined as

$$E(V) = E_0 + K_0 V_0 \left[ \frac{1}{K_0'(K_0' - 1)} \left( \frac{V^{1-K_0'}}{V_0} \right) + \frac{1}{K_0'} \frac{V}{V_0} - \frac{1}{K_0' - 1} \right] \tag{2.30}$$

where $K_0$ is the modulus of incompressibility, $K_0'$ is the first derivative of $K_0$ with respect to the pressure, $V$ is the final volume and $V_0$ is the volume not compressed. If the reduction of volume under compression is low, *i.e.*, for $\frac{V}{V_0}$ greater than 90%, the Murnaghan equation can model experimental data with satisfactory accuracy.

### Infrared- and Raman Spectra

Nowadays, computational spectroscopy can complement experimental spectroscopy to determine the nature of of some systems of interest. In general, infrared- and Raman spectroscopy[42] occupy a prominent role in material science study, due to their versatility and reliability. The IR and Raman simulations, despite the prediction power, cannot unfortunately reproduce in full details the experimental spectra, due to the intrinsic approximations that are made in the implementation of the techniques in the codes. as it will be explained below. Nonetheless, these two complementary methodologies are extremely useful when investigating the properties of molecules and solids. Within the Born-Oppenheimer (BO) framework, where electronic and nuclear motions are decoupled, the potential energy surface represents the sum of many electronic energy contributions for many nuclear conformation

$$\mathcal{E}_{\text{PES}}(\mathbf{R}) = \hat{V}_{NN} + \mathcal{E}_{\text{e}}(\mathbf{R}) = \sum_{A=1}^{M} \sum_{B>A}^{M} \frac{Z_A Z_B}{r_{AB}} + \mathcal{E}_{\text{e}}(\mathbf{R}) \tag{2.31}$$

where $\mathcal{E}_{\text{PES}}(\mathbf{R})$ is the total energy of the system for many nuclear conformations, $\hat{V}_{NN}$, see eq. (2.6), is the internuclear repulsion potential operator and $\mathcal{E}_{\text{e}}(\mathbf{R})$ the electronic energy for a set of coordinates $\mathbf{R}$. Once the electronic problem is solved, then the Schrödinger equation for nuclei can consequently be solved. The nuclear Hamiltonian that is used in the description of the nuclei motions is

$$\hat{H}_{\text{nuclei}} = \hat{T}_N + \mathcal{E}_{\text{PES}} = -\sum_{A=1}^{M} \frac{1}{2M_A} \nabla_A^2 + \mathcal{E}_{\text{PES}}(\mathbf{R}) \tag{2.32}$$

where $\hat{T}_N$ is the nuclear kinetic energy. It follows that, within the BO framework, nuclei are moving on a PES obtained by solving the electronic problem. The solution of $\hat{H}_{\text{nuclei}}$ is $\Psi_{\text{nuclei}}(\mathbf{R})$, which describes the motion of nuclei like vibration, rotation and translation. Generally, the complete PES is unknown since only a small fraction of the electronic energy terms is estimated as a function of the coordinates position $q$; despite this limitation, what is exactly known, at the end of a geometrical optimization, are indeed the atomic coordinates for which the first derivative of the potential term with respect to the position is 0, that is

$$\frac{\partial \mathcal{E}_{\text{PES}}}{\partial q_1} = \frac{\partial \mathcal{E}_{\text{PES}}}{\partial q_2} = ... = \frac{\partial \mathcal{E}_{\text{PES}}}{\partial q_n} = 0 \tag{2.33}$$

This conditions assures that the optimization has converged in a minimum of the PES, which might be local or global, despite not knowing the real for of the PES. Thus, to obtain an expression to use in the nuclear Hamiltonian, several approximation needs to be accounted, the most important of which is the *harmonic approximation* one.

In IR spectroscopy, the main phenomenon of interest is the vibrational motion of a chemical bond. Considering the simplest case of a biatomic molecule, where its equilibrium bond distance is $r_{\text{eq}}$ corresponding to the energy minimum of the system, the Taylor expansion of potential energy term $\mathcal{E}_{\text{PES}}(r)$, rewritten as $U(r)$ for convenience, is

$$U(r) = U(r_{\text{eq}}) + \left.\frac{dU}{dr}\right|_{r=r_{\text{eq}}} (r - r_{\text{eq}}) + \frac{1}{2!}\left.\frac{d^2U}{dr^2}\right|_{r=r_{\text{eq}}} (r - r_{\text{eq}})^2 + ... \tag{2.34}$$

if the value of $U(r_{\text{eq}})$ is equal to 0, knowing that for $r = r_{\text{eq}}$ the minimum of the PES is found and that, as a consequence, the first derivative is also equal to 0, it follows that the first two terms of the Taylor series go to 0. The truncation at the second order term of eq. (2.34) is a parabolic curve

$$U'(r) = \frac{1}{2}\left.\frac{d^2U}{dr^2}\right|_{r=r_{\text{eq}}} (r - r_{\text{eq}})^2 \tag{2.35}$$

where

$$k = \left.\frac{d^2U}{dr^2}\right|_{r=r_{\text{eq}}} \tag{2.36}$$

is the force constant. For a general biatomic molecule XY, the Schrödinger equation for the nuclear motion can be written as

$$\left[ -\sum_k \frac{1}{2m_k} \nabla_k^2 + \frac{1}{2}\left.\frac{d^2U}{dr^2}\right|_{r=r_{\text{eq}}} (r - r_{\text{eq}})^2 \right] \Psi_{\text{nuclei}}(\mathbf{R}) = E_{\text{vibr}}\ \Psi_{\text{nuclei}}(\mathbf{R}) \tag{2.37}$$

By using the reduced mass term[2] $m^*$ for the generic biatomic XY molecule, eq. (2.37) can be rewritten as

$$\left[-\frac{1}{2m^*}\frac{d}{dr^2} + \frac{1}{2}\frac{d^2U}{dr^2}\bigg|_{r=r_{\text{eq}}}(r-r_{\text{eq}})^2\right]\Psi_{\text{nuclei}}(\mathbf{R}) = E_{\text{vibr}}\ \Psi_{\text{nuclei}}(\mathbf{R}) \tag{2.38}$$

In eq. (2.38) it can be noticed the appearing of the second derivative of the potential energy term $U(r_{\text{eq}})$. Reformulating the Schrödinger equation for the nuclear motion that accounts for the Taylor expansion truncated at the second order can be generalized as

$$\left[-\sum_k \frac{1}{2m_k}\nabla_k^2 + \frac{1}{2}(\mathbf{R}-\mathbf{R}_{\text{eq}})H_{\text{eq}}(\mathbf{R}-\mathbf{R}_{\text{eq}})\right]\Psi_{\text{nuclei}}(\mathbf{R}) = E_{\text{vibr}}\ \Psi_{\text{nuclei}}(\mathbf{R}) \tag{2.39}$$

being $\mathbf{R}$ the vector for a generic set of coordinates, $\mathbf{R}_{\text{eq}}$ the set of coordinates at the equilibrium position and $H_{\text{eq}}$ the Hessian matrix, *i.e.*, the matrix of the second derivative of the potential energy $U$ with respect to the atomic coordinates, evaluated for the equilibrated geometry. The eigenvalues associated with the wavefunction $\Psi_{\text{nuclei}}$ provide the vibrational levels of the system. For a certain vibrational mode $m$

$$\mathrm{E}_{\text{vibr}}^m = \left(n + \frac{1}{2}\right)h\omega_m \quad \text{with} \quad n = 0, 1, 2, ... \tag{2.40}$$

where $n$ represents the vibrational quantum number. The selection rules that hold for the harmonic approximation allow for transitions to occur with $\Delta n = \pm 1$, that translate in a vibrational energy equal to

$$\Delta\mathrm{E}_{\text{vibr}}^m = h\omega_m \tag{2.41}$$

where $\omega_m$ is the frequency associated to the vibrational mode $m$. For a non-linear molecule of $N$ atoms, there are 3$N$-6 vibrational modes[3], 3$N$-5 if the molecule is linear. The eq. (2.39) holds if some conditions are met, specifically

#1 eq. (2.39) is only valid for minima and saddle points, *i.e.*, the IR simulation is valid only for an optimized geometry, not for an arbitrary non-optimized structure.

#2 The most computationally expensive part of an IR simulation is the estimate of the Hessian matrix, and it has to be solve at the same level of theory used for the geometry optimization within the same computational framework (*e.g.* not mixing plane waves and all-electron basis set).

#3 The appearing of a single negative frequency in the IR spectrum is symptomatic of the fact that the structure considered belongs to a transition state (saddle point) and not a minimum of the PES. On the contrary, absence of any negative frequency means the system is in a minimum of the PES.

---

[2] The reduced mass term, $m^*$, for a biatomic XY molecule is defined as

$$-\sum_k \frac{1}{2m_k}\nabla_k^2 = -\left(\frac{1}{2m_{\text{A}}}\frac{d^2}{dr^2} + \frac{1}{2m_{\text{B}}}\frac{d^2}{dr^2}\right) = -\frac{1}{2}\frac{m_{\text{A}}+m_{\text{B}}}{m_{\text{A}}m_{\text{B}}}\frac{d^2}{dr^2} = -\frac{1}{2m^*}\frac{d^2}{dr^2}$$

[3] Each non-linear molecule composed on $N$ atoms has 3$N$ degrees of freedom, six of which are translation and rotations of the molecule itself.

4 The selection rule $\Delta n = \pm 1$ is only valid for the harmonic approximation; this translates on the fact that, in calculated spectra, some peaks might be missing with respect to the real one.

The intensity ($I$) of the peaks in a simulated IR spectrum is proportional to the square of the transition dipole moment $\mu$ as

$$I \propto |\mu^m|^2 \tag{2.42}$$

which, in turn, it can be approximate as

$$\mu^m = \frac{d\mu}{dq} \int \Psi^{\mathrm{ex}} q \Psi^{\mathrm{gr}} dq \tag{2.43}$$

where $\Psi^{\mathrm{ex}}$ and $\Psi^{\mathrm{gr}}$ are the wavefunctions for the excited- and ground-state configuration, respectively. As such, the intensity $I$ is strongly dependent upon the transition dipole moment variation of the system associated to the same vibration. A vibration that does not change the transition dipole moment will result *inactive* in the IR. Computationally, the intensity of the IR vibrational are estimated by calculating the second derivative of the energy *w.r.t.* the nuclear motion and an external electric field $F$, since the dipole moment is the first derivative of the energy *w.r.t.* $F$

$$I_{\mathrm{IR}} \propto \left(\frac{d\mu}{dq}\right)^2 \rightarrow I \propto \left(\frac{d^2U}{\partial F \partial q}\right)^2 \tag{2.44}$$

A complementary technique to the IR is the Raman spectroscopy, where the selection rule requires that the polarizability $\alpha$ of the system must change during the vibrational motion. The intensity of the Raman spectra requires the calculation of the third derivative of the energy *w.r.t.* nuclear motion and the electric field $F$

$$I_{\mathrm{RM}} \propto \left(\frac{d\alpha}{dq}\right)^2 \rightarrow I \propto \left(\frac{d^3U}{\partial F^2 \partial q}\right)^2 \quad \text{where} \quad \alpha = \frac{\partial^2 U}{\partial F^2} \tag{2.45}$$

**The Supercell Approach**

The supercell method is a ubiquitous method for studying solid-state system in the periodic boundary conditions approach. This is particularly useful when considering the formation of doped systems or systems with defects, vacancies etc.. This approach allows to reach, on one side, a more realistic picture of the compound under investigation, resembling the experimental arrangement of the material; this is particularly useful when the doping or the defect formation are found experimentally to be in the very low concentrations. On the other hand, when applying the supercell approach, defects and doping species are found at sufficiently long distances to not interact with each other, and this is extremely important to model realistic conditions. In this work the supercell approach will be employed to study the doped structures of $BaTiO_3$ at 25% and 50% respectively, giving the chance to highlight similarities and differences between the structures and the subsequent modifications that the doping species induce.

# Chapter 3

# Computational Investigation of BaTiO$_3$

The computational investigation of solid-state system requires to benchmark some parameters, in particular when dealing with periodic codes based on plane waves. The study hereby presented is based on the comparison, in terms of structural and electronic properties, obtained by employing the plane wave Quantum Espresso v.7.0 code[43, 44] (open source), mainly developed at the Scuola Internazionale di Studi Avanzati (SISSA) with respect to the proprietary CRYSTAL14[45, 46], developed at the University of Torino, which instead is based on GTO basis set.

# 3.1 Accuracy and Convergency Tests

The key goal of the convergence tests is to assess the best set of parameters to employ in the simulation to achieve a good compromise between computational cost and accuracy. In this work, this analysis is partially carried out on the inputs of the Quantum Espresso code. The selected structure for testing purposes is the unit cell of the cubic $BaTiO_3$, downloaded from The Materials Project Repository repository[1].

**Table 3.1:** Fractional atomic coordinates of the pristine cubic $BaTiO_3$ system.

| Atom | X | Y | Z |
|------|-----|-----|-----|
| Ba | 0.0 | 0.0 | 0.0 |
| Ti | 0.5 | 0.5 | 0.5 |
| O | 0.0 | 0.5 | 0.5 |
| O | 0.5 | 0.0 | 0.5 |
| O | 0.5 | 0.5 | 0.0 |

The fractional atomic coordinates of the BTO system are reported in table 3.1, with the $a = b = c$ lattice parameters equal to 4.036 Å, while $\alpha = \beta = \gamma = 90°$. The space group, as already mentioned above, is $Pm\bar{3}m$. The crystal system has been refined by means of the XRD diffractometry and scanning electron microscopy[47]. The benchmark is performed by employing the PWscf ToolKit[2], a code that interfaces with Quantum Espresso allowing to operate a systematic change of a parameter at a time, so that to systematically investigate the influence of the same with respect to the system considered.

**Convergence test of the lattice parameter**

The lattice parameter of the cubic $BaTiO_3$ is made varying in the around of the reference/experimental one, keeping fixed the atomic positions. The resulting total energy *vs* lattice parameter plot, see fig. 3.1, provides a reasonable guess on the equilibrium lattice parameter that should be expected after convergence. The dataset forming the classic parabolic trend of these graphs can subsequently be fitted with a Birch-Murnaghan equation of stateeq. (2.30), which will provide a guess for the Bulk modulus to be later compared with experiment. The resulting plot, fig. 3.1, for $BaTiO_3$ shows that the minimum of the parabola is set around ∼3.9 Å, as expected. As such, the lattice parameter highlighted with the yellow star is the our choice for all the subsequent calculations.

---

[1] Last access performed on February 2022 at https://materialsproject.org/materials/mp-2998/
[2] http://pwtk.ijs.si/index.html
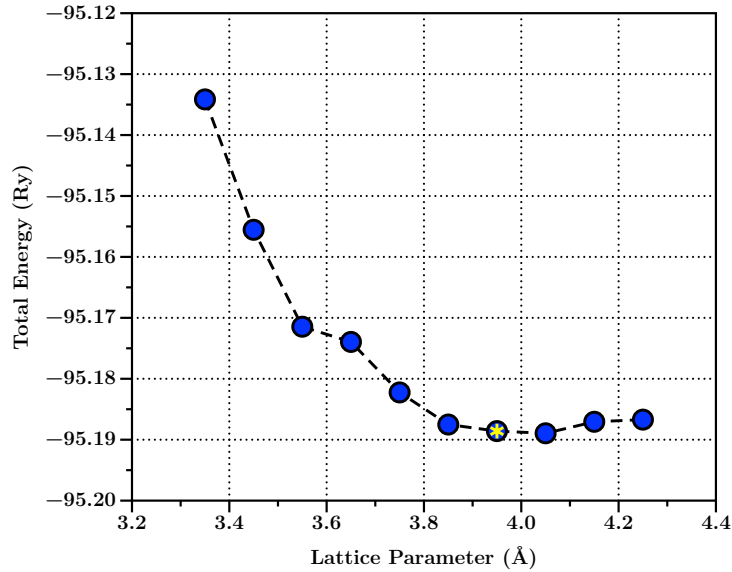
**Figure 3.1:** Total energy *vs*. lattice parameter variation. The yellow star shows the selected value for the $BaTiO_3$ system

### Convergence test of the kinetic energy cutoff

Convergence test for the energy cutoff employed for the ONCV pseudopotentials[48, 49]. This test is performed by keeping fixed the lattice parameter to an ideal value obtained from step (1), while the kinetic energy cutoff is made varying from low (30 Ry) to high (90 Ry) values and plot against the corresponding total energy of the system. From fig. 3.2 it can be seen that the asymptotic behavior is reached at around 60 Ry. This value, highlighted with a yellow star in the fig. 3.2, was selected for the whole set of calculations reported in this work done via QE.
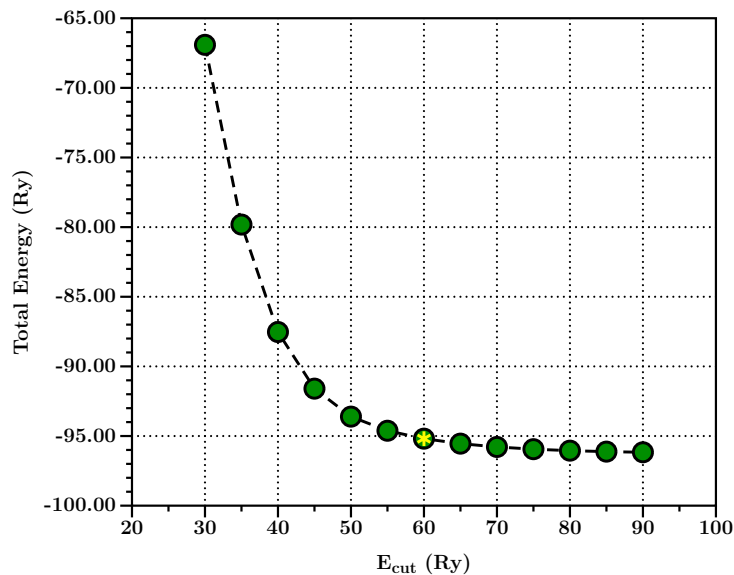


**Figure 3.2:** Total energy *vs*. $E_{cut}$ variation. The yellow star display the selected value to employ.

**Convergence test on the $\vec{k}$-points**

This test is performed to evaluate which is the smallest integration grid that should provide accurate data at a reasonable computational cost. The plot in fig. 3.3 shows that convergence is basically achieved with a 4x4x4 grid, equivalent to 10 $\vec{k}$-points. The use of a larger number of $\vec{k}$-points would make the calculation increasingly expensive with little gain in terms of accuracy. As such, the 4x4x4 grid is selected for the actual study of BTO.
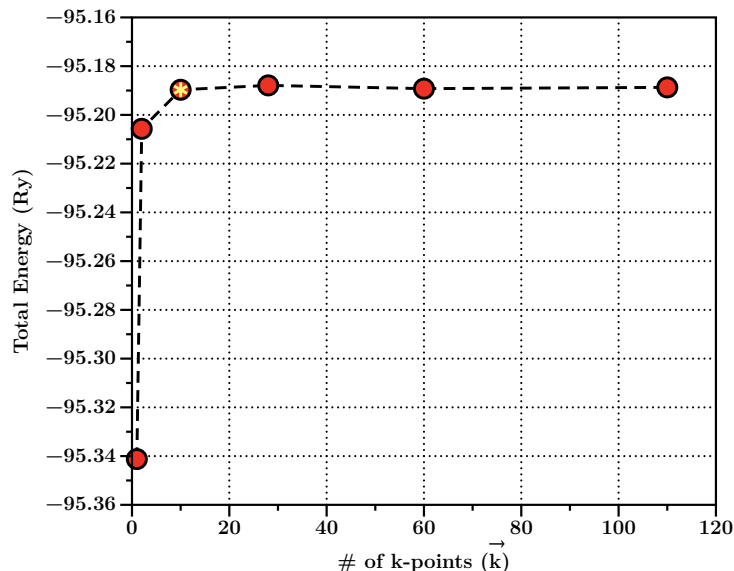


**Figure 3.3:** Total energy *vs.* $\vec{k}$-points. The star shows the selected point, corresponding to a 4x4x4 grid.

## 3.1.1 Gaussian Type Orbitals

The selection of the GTO basis set for the Crystal14 code is mainly based on the reference literature available for the study of $BaTiO_3$ and related systems. Specifically, a non-exhaustive collection of all-electron and effective core potentials (ECP) are available at Crystal - Basis Set Library[3]. In case of the BTO, optimized all-electron and ECP basis set are currently available.

---

[3]  https://www.crystal.unito.it/basis-sets.php

## 3.1.2 Summary of the Computational Settings

**Quantum Espresso - Plane Waves basis set code**

The DFT simulations with the plane waves basis set have been performed by employing the Quantum Espresso[43, 44] suite of code, version 7.0. The Perdew-Burke-Ernzerhof (PBE) approximation is used for the exchange and correlation functional terms. The ONCV norm-conserving pseudopotentials are employed for the atomic species, with a kinetic energy cutoff of 60 Ry. To improve the convergence, the Marzari-Vanderbilt "cold" smearing parameter of 0.015 Ry is employed. The structural relaxations for the lattice and atomic positions are converged when forces are found below than $10^{-6}$ Ry/Bohr, with the electronic total energy differences of $10^{-8}$ Ry. While the pristine $BaTiO_3$ is modeled as a single unit cell, the doped structures are modeled throughout a supercell approach, by expanding the optimized 1x1x1 unit cell in a 1x1x2 (for the 50% doped systems) and 1x2x2 (for the 25% doped crystals), respectively. The supercells are then subsequently re-optimized in order to equilibrate the forces induces by the substitution of the Strontium and Tin atoms in spite of Barium and Titanium ones, respectively. The electronic structure properties, *i.e.*, DOS and band structure, of the 1x1x1 cell and 1x1x2 and 1x2x2 supercells are then studied both at PBE and PBE0[4] (hybrid functional) level of theory[50, 51].

**CRYSTAL14 - Gaussian Type Orbitals basis set code**

The DFT calculations based on the all-electron basis set and effective core pseudopotentials have been performed by employing the CRYSTAL14[45, 46] package, using both the PBE and hybrid PBE0 functionals. The former functional is used, once more, for the optimization of the same set of structures reported above, while the latter functional for the calculation of the corresponding electronic properties, that is DOS and band structure. In all the calculations the atomic centers are described by the ones developed and tested by Baranek and co-workers[52] for the BTO, where the Oxygen and Titanium are all-electron, while the Barium is Hay-Wadt small-core pseudopotential (ECP)[53–55]. The electronic integration is performed by using a 8x8x8 Monkhorst-Pack[56] $\vec{k}$-point mesh for the pristine and doped supercells. The accuracy of the Coulomb and exchange integrals calculations is controlled by setting the threshold to 8, 8, 8, 8, and 16 values, while the remaining set of parameters for the geometrical convergence is kept to $10^{-4}$ for maximum gradient, $5\times10^{-5}$ for root-mean square of the gradient, $2\times10^{-4}$ for both maximum and root-mean square of the displacement, respectively. In all cases, the both the lattice parameters and atomic positions are optimized at PBE level.

---

[4] The PBE0 hybrid functional mixes Hartree-Fock exchange energy ($E_x^{\mathrm{HF}}$) with PBE exchange energy ($E_x^{\mathrm{PBE}}$) in a 1:3 ratio, along with the full PBE correlation energy ($E_c^{\mathrm{PBE}}$) as

$$E_{xc}^{\mathrm{PBE0}} = \frac{1}{4}E_x^{\mathrm{HF}} + \frac{3}{4}E_x^{\mathrm{PBE}} + E_c^{\mathrm{PBE}}$$

The thesis presented here, as already mentioned, is an explorative work for assessing the quality in the use of the plane waves *vs.* GTO basis sets. The use of the PBE functional for investigating both the structural and electronic properties, the latter ones compared with the results at a hybrid level (*i.e.*, PBE0), are then intentional. The author is aware of the fact that GGA functionals underestimate the band gap in solids due to self-interaction, which in PBE0 is partially compensated by introducing a fix amount of exact exchange. Despite the intrinsic limits that PBE presents, it is still probably one of the most popular functionals in use today and, for the goals outline in the introductory part, it fully satisfies our requirements. More detailed investigations are already ongoing in order to refine the computational settings and methods to properly study the class of systems presented in this work, by making use, for instance, of other hybrid functionals like B3LYP.

### 3.1.3 Optimized BaTiO₃ Unit Cell

The optimization of the BTO unit cell performed with QE and CRYSTAL displays similarities and differences that might be recasted to the different basis set employed in the two codes. Specifically, table 3.2 summarizes the optimized structures at PBE level of theory calculated in this work, the experimental value and previously reported values, and the resulting percentual error[5] (PE)

**Table 3.2:** The relaxed structures of the cubic BTO obtained in this work compared to the experimental data and prior theoretical results from literature and corresponding percentual errors.

| Phase | Source | Lattice Constant $a$ (Å) | PE % |
|-------|--------|--------------------------|------|
| Cubic | Exp.[57] | 4.000 | - |
|  | This Work - PW | 3.934 | -1.650 |
|  | This Work - CRY14 | 4.179 | 4.475 |
|  | [58] | 4.000 | 0.000 |
|  | [59] | 4.030 | 0.750 |
|  | [60] | 4.006 | 0.150 |
|  | [61] | 3.943 | -1.425 |

It can be observed that, while in the case of the plane waves basis set the lattice parameter $a$ is of the same order of 3.943 Å as reported by Ghosez and co-workers[61], and only slightly underestimated the experimental value. Meanwhile, the results for the lattice parameter obtained via GTO basis set seems to overestimate and expand the unit cell of $\sim 4.5$ %. This cell expansion can be related, in first approximation, to the formulation of the GTO basis set that leads to potential dispersion effect arising from the outers shells of the GTO basis used for Ba, Ti and O. Despite these differences, it can be seen the order of magnitude of the lattice parameter is capture within the 5% error of accuracy. The average Ba-Ti distance in the PW optimized structure is 3.407 Å, while for the GTO optimized one is 3.619 Å, with a difference of 0.2. The same difference is found if considering the average distance between Ba (0,0,0) with respect to O $(0,\frac{1}{2},0)$. Due to these geometrical distortion arising from the two methods, it can be expected the electronic properties will also be partially affected.

---

[5] The percentual error is estimated as

$$\frac{(\text{Calculate Value} - \text{Reference Value})}{\text{Reference Value}} * 100$$

## 3.1.4 Band Structure

The band structures plot for the BTO system have been calculated with both methods and compared, as reported in fig. 3.4. The same format of the images is also used for the doped cells. Specifically, the band structure calculated *via* plane wave pseudopotential method displays the valence band with black- and the conduction one with dashed-orange lines, respectively. The projection onto the corresponding DOS is also shown for completeness. The red and green lines identify the VBM and CBM, respectively, and the corresponding band gap is highlighted in purple. Conversely, because the use of CRYSTAL14 is tightly linked to the used of a specific visualization software (CRYSPLOT) for the post-processing analysis of the output files, the rendering of the corresponding band structure is lower. Despite this, the distribution of the valence and conduction bands are clear and they can be compared with the counterpart from Quantum Espresso.
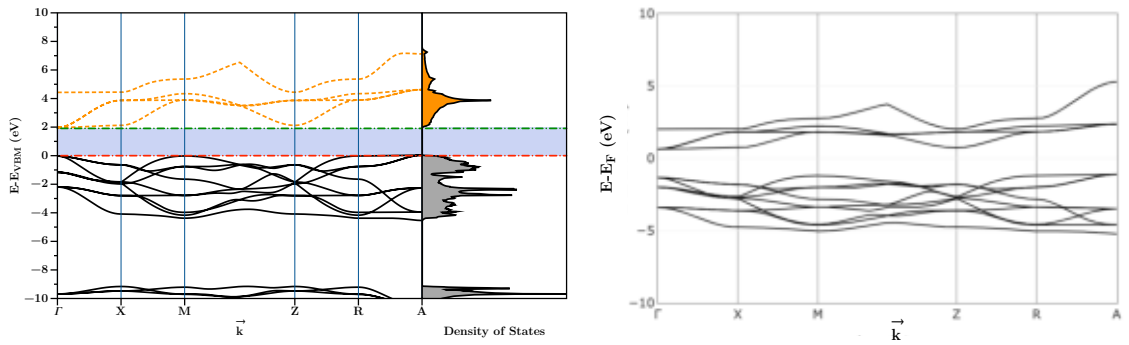


**Figure 3.4:** Left - Band structure calculated with the plane waves PW method. Right - Band structure calculated with the GTO basis set.

At first, by analyzing the two band structure plots, it can be seen that both present the same trend for the few bands right below the VBM and right above the CBM, with respect to the chosen $\vec{k}$-path $\Gamma$-*X*-*M*-*Z*-*R*-*A*. While from these plot is it not possible to elucidate the different contributions coming from the different atomic species, nonetheless a direct comparison with reported literature can help to interpret them.
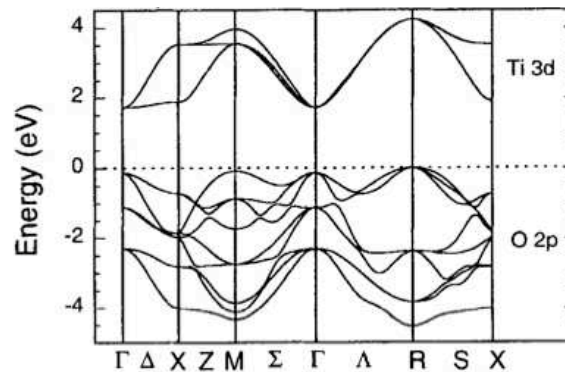


**Figure 3.5:** Electronic band structure of cubic BTO along different high symmetry point as taken from Ghosez[61]

The band structure depicts the distribution of the energies as function of the different atomic contributions. It can be seen that the conduction band major contribution comes from the 3*d* orbitals of $Ti^{4+}$ atom, while the valence band is mainly generated by the 2*p*

orbitals of the oxygen atoms, as reported by Ghosez in fig. 3.5. More detailed analysis have demonstrated a partial hybridization between the O $2p$ and Ti $3d$ orbitals in these systems, which is reflected on the Ti charges that oscillates between 2.5 to 3. Pertosa[62] instead found that Ba has only a minor contribution to the band structure distribution, mainly influencing the interactions at a deeper energetic level. The estimate of the band gap is not unique because it depends on the initial reference $\vec{k}$-path provided in the sampling of the reciprocal space. In the both the plane waves and GTO calculation carried out in this work the following coordinates for the high-symmetric $\vec{k}$-points are used: $\Gamma$ (0,0,0), $X(\frac{1}{2},0,0)$, $M(\frac{1}{2},\frac{1}{2},0)$, $Z(0,0\frac{1}{2})$, $R(\frac{1}{2},0,\frac{1}{2})$ and $A(\frac{1}{2},\frac{1}{2},\frac{1}{2})$, and these might differ with respect to those reported by Ghosez and co-workers. For sake of completeness, in table 3.3 are reported the whole set of relevant band gaps estimated with the two methods here employed.

**Table 3.3:** Band gaps calculated for $BaTiO_3$ at PBE level of theory for different high-symmetry $\vec{k}$-path points.

| Source | Type of Gap | $\vec{k}$-path | Gap (eV) |
|---|---|---|---|
| This work - PW | Indirect | $M \rightarrow \Gamma$ | 1.99 |
| This work - PW | Indirect | $R \rightarrow \Gamma$ | 1.99 |
| This work - PW | Direct | $\Gamma \rightarrow \Gamma$ | 2.02 |
| This work - CRY14 | Indirect | $M \rightarrow \Gamma$ | 1.84 |
| This work - CRY14 | Indirect | $R \rightarrow \Gamma$ | 1.84 |
| This work - CRY14 | Direct | $\Gamma \rightarrow \Gamma$ | 1.97 |

Ghosez and co-workers reported an indirect $R \rightarrow \Gamma$ band gap of 1.72 eV and a $\Gamma \rightarrow \Gamma$ direct one of 1.84 eV, but at a LDA level of theory, which generally performs even worse *w.r.t.* GGA. However, the ratio between indirect and direct gaps, within the same methodology, is equal to $\sim 0.9$ in all the cases, proving that the results here presented are aligned with those reported in literature. It can be noted from table 3.3 that, despite the 0.2 eV difference in $M \rightarrow \Gamma$ and $R \rightarrow \Gamma$ between PW and GTO basis set, the values are consistent among them, that is, it should be a warning that the comparison between different methodologies can be dangerous and misleading if not correctly handled. The direct comparison with experiment cannot be done at this level of theory due to DFT misfit[6]. The actual experimental value for the band gap that is generally accepted for pristine $BaTiO_3$ is set to 3.2 eV, as estimate by Wemple[63], and it is attributed to the direct $\Gamma \rightarrow \Gamma$ point.

---

[6] The discrepancy only involves excitation energies, but it does not influence the accuracy obtained for the ground-state properties.

### 3.1.5 Density of States

A complementary analysis carried out to show similarities and differences not only between PW and GTO, but also between GGA and hybrid functionals (within the method), is the plotting of the DOS normalized with respect to the intensity, as reported in fig. 3.6.
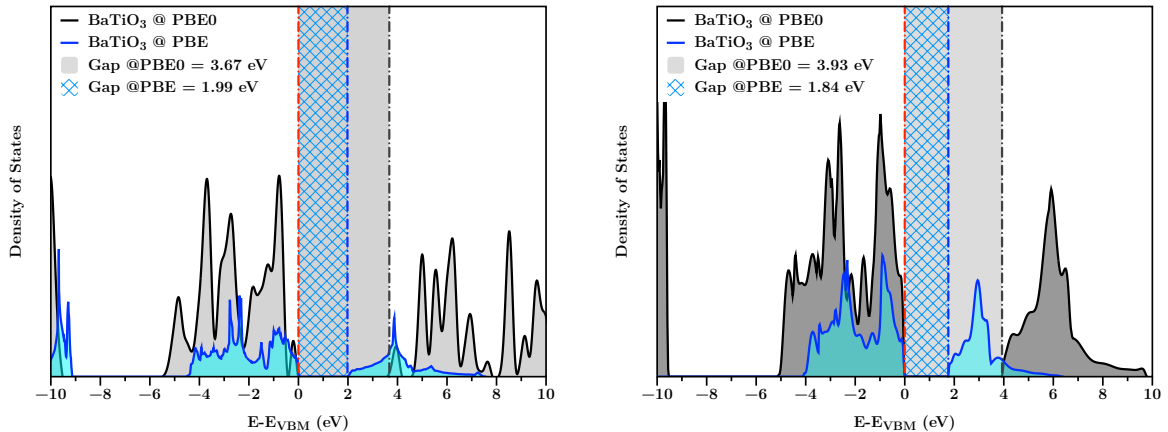


**Figure 3.6:** Left - DOS calculated at PBE and PBE0 level of theory with PW. Right - DOS calculated at PBE and PBE0 level of theory with GTO. In both cases the blue line and grid highlight the PBE DOS and the corresponding gap; the same happens for the black line and grey area, which instead put in evidence the PBE0 DOS and corresponding gap.

The corresponding PBE band gaps are also obviously found here. What is instead interesting to notice is how the gap opens up when using the PBE0 functional in both cases, with a gap of 3.67 eV for the PW case and 3.93 eV for the GTO ones. The 0.3 eV difference between the two depends upon the implementation of the functional and, once more, on the difference formulations for the basis set employed. In both cases the gaps, if compared with the experimental one of 3.2 eV reported by Wemple, is overestimating it, a behavior found also in case of the B3LYP functional as reported by Piskunov and co-workers[59], where they adopted an older version of CRYSTAL code, *i.e.*, CRYSTAL09[64]. In this sense, the PW approach performs slightly better. The careful comparison of the PBE0 results shows that, in the case of the PW approach, two small peaks can be detected, one at 0 eV and the other centerer at 4 eV, respectively. These two small peaks might be the result of the introduction of the exact exchange throughout the PBE0 functional. Unfortunately, due to some missing terms in the original ONCV pseudopotentials used in this work, the projection of the single contributions to each band is not available at the moment. This lack of information is also valid for the doped cells. A more detailed analysis is already ongoing on this aspect.

# Chapter 4

# BaTiO$_3$-doped System

In this chapter the results for the doped structures of BaTiO$_3$ with strontium (Sr) and tin (Sn) are presented. In particular, the systems considered here feature a 25% and 50% doping for both Sr$^{2+}$ and Sn$^{4+}$. In this chapter firstly the data for the Sr doping are presented, then it follows the presentation of the data for the Sn doping, respectively. Specifically, for each doped system, a comparison between structural optimized parameters, band structures and density of states will be presented and commented and, whenever possible, compared with the available experimental or theoretical data from literature.

# 4.1   Ba$_{(0.50)}$Sr$_{(0.50)}$TiO$_3$

The doping of BaTiO$_3$, and systems of formula ABO$_3$ resembling the perovskite, has found great interest over the years due to the possibility of manipulating structural and electronic properties which might have an enormous repercussion on industry and, in general, technology. That is, the solid solution of BaTiO$_3$ with SrTiO$_3$ results in the barium strontium titanate, which is thought to be a promising material for its dielectric properties. The tuning of the mole ratio between Ba and Sr can fine tune several properties meeting a variety of applications that can range from capacitors to phase shifters and else. Both the starting structures feature a cubic phase at high temperature, facilitating the substitutional process. The doping procedure is done by means of the supercell approach. The optimized BTO unit cells obtained with PW and GTO basis set are expanded as 1x1x2, containing each one 10 atoms, as shown in fig. 4.1. The Ti$^{4+}$ atoms are coordinates with 6 oxygen atoms, which produces an octahedral TiO$_6$ cluster. At the same time, Ba and Sr are coordinated with 12 O atoms, which results in a BaO$_{12}$ and SrO$_{12}$ clusters. The
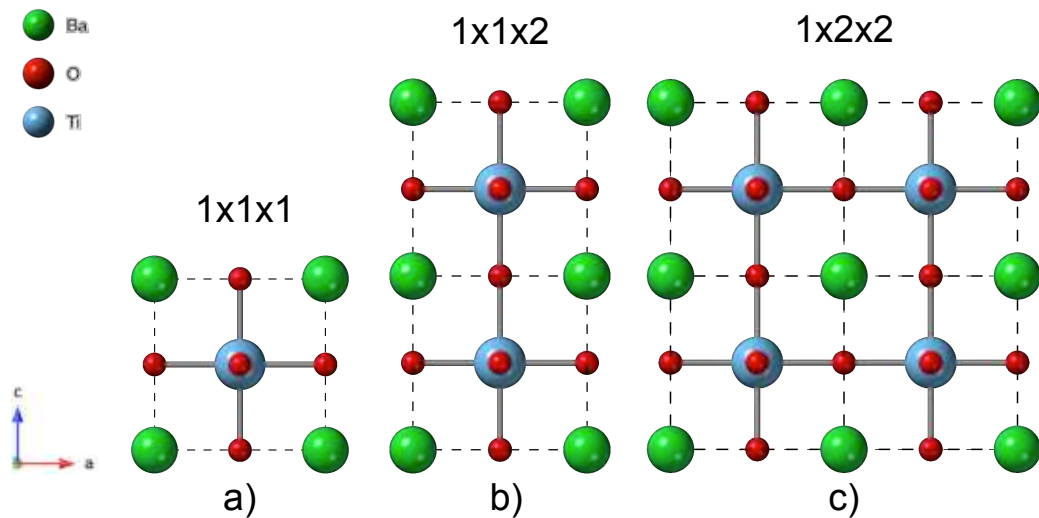


**Figure 4.1:** Schematic representation of the propagation of the BaTiO$_3$ (*a*) unit cell to build up the (*b*) 1x1x2 and (*c*) 1x2x2 supercells.

analysis of the lattice parameters optimized for the lattice constant of the 1x1x2 supercells shows that the one from GTO overestimate of about 4.3% the experimentally determined value. On the contrary, the cell optimized at the same level of theory with plane waves basis set shows a compression of $\sim$-1.5% with respect to the experimental lattice. Both the calculations are in agreement with the experimental results, although it might be expected that the GTO ones could be further refined.

**Table 4.1:** The relaxed structures of the $Ba_{(0.50)}Sr_{(0.50)}TiO_3$ 1x1x2 supercells obtained in this work compared to the experimental data, prior theoretical results from literature and corresponding percentual errors

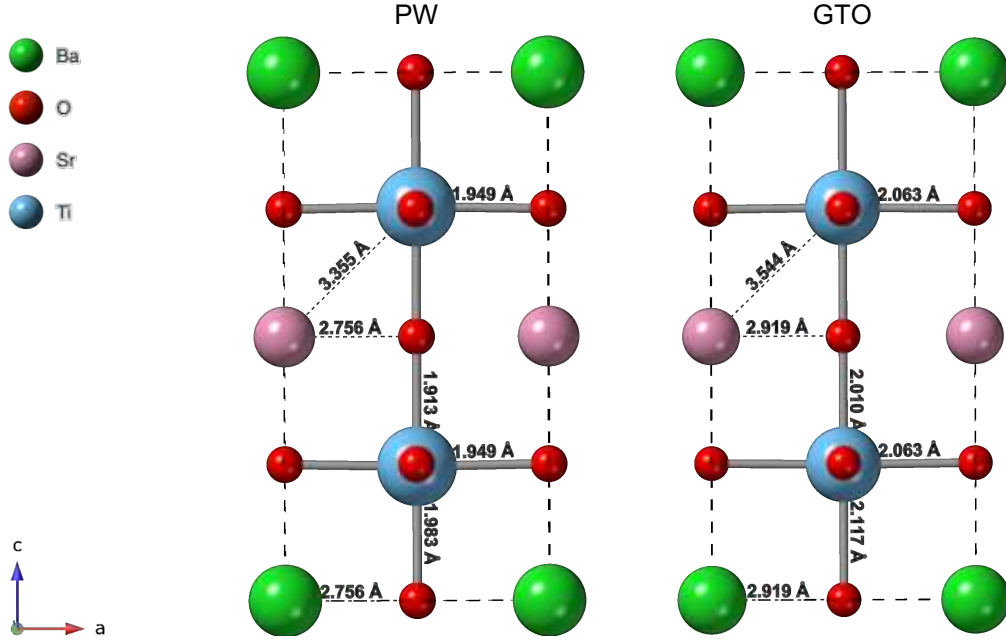| Phase | Source | Lattice Constant $a=b$ (Å) | PE % |
|-------|--------|---------------------------|------|
| Cubic | Exp.[65] | 3.957 | / |
| | This Work - PW | 3.898 | -1.491 |
| | This Work - CRY14 | 4.127 | 4.296 |
| | [65] | 3.939 | -0.455 |



**Figure 4.2:** Plane waves (PW) and Gaussian Type Orbitals (GTO) optimized structures of the 1x1x2 supercell of $Ba_{(0.5)}Sr_{(0.5)}TiO_3$.

The detailed analysis of the optimized structures reported in fig. 4.2 marks similarities and differences between the two computational method employed. Specifically, analyzing the Ti-O bonds, it can be noticed that in both cases (PW and GTO), in the surrounding of the Sr atom the stretching of Ti-O bond on one side and the complementary elongation from the opposite one occurs, with current values as 1.983 Å to 1.913 Å for the PW case, and 2.117 Å to 2.010 Å in the GTO one. These differences in the Ti-O bonds generate a "compressed" octahedral cluster, with Ti atoms in the center. Notice that the unaffected Ti-O bond is of the order of 1.949 Å. Despite the fact that the GTO supercell displays larger values of bonds, the influence of the doping species can still be properly accounted. A general analysis of the other interaction with the cells shows that, in average, the Sr-Ti bond distances are 3.355 Å for PW and 3.544 Å for GTO. The complete list of relevant bonds is reported in table 4.2, with the corresponding percentual error[1] between them. It can be seen that the GTO method tends to overestimate the bond of approximately 5.1%

---

[1] The percentual error is estimated as

$$\frac{(\text{GTO value} - \text{PW Value})}{\text{PW Value}} * 100$$

to 6.8%, with respect to PW.

**Table 4.2:** Comparative table of the most important bond distances obtained by using PW and GTO methods and corresponding percentual errors.

| Bonds | PW (Å) | GTO (Å) | PE (%) |
|-------|--------|---------|--------|
| Ti-O  | 1.949  | 2.063   | 5.849  |
| Ti-O  | 1.983  | 2.117   | 6.757  |
| Ti-O  | 1.913  | 2.010   | 5.071  |
| Ba-O  | 2.756  | 2.919   | 5.914  |
| Sr-O  | 2.756  | 2.919   | 5.914  |
| Sr-Ti | 3.355  | 3.544   | 5.633  |

## 4.1.1 Band Structure

The band structure investigation of the system with both PW and GTO shows approximately the same behavior at the upper energy levels of the VBM and CBM, respectively. In the PW band structure the gap is highlighted with a purple horizontal bar, separating the valence band (black lines below 0 eV) from the conduction band (orange-dashed lines) found above 0 eV. The contributions to the single energy levels cannot be distinguished neither in the PW case not in the GTO one. However, the introduction of the Sr atom in such high percentage is believed to promote some intermediate electronic levels that might mix with the Ba ones at a deeper energy level. On the other hand, from the structural analysis, it could be observed that introducing Sr at 50% doping has a direct impact on the local structural arrangement of the BaTiO$_3$ supercell, which will be reflected on the its electronic structure. Whilst the $\vec{k}$-path is defined in the same way in both PW and GTO cases, the projection of the bands displays that, in the former case the indirect gap is found between $R{\rightarrow}\Gamma$, while in the latter between $M{\rightarrow}\Gamma$. The corresponding values are 1.96 eV for PW and 1.78 eV for GTO.
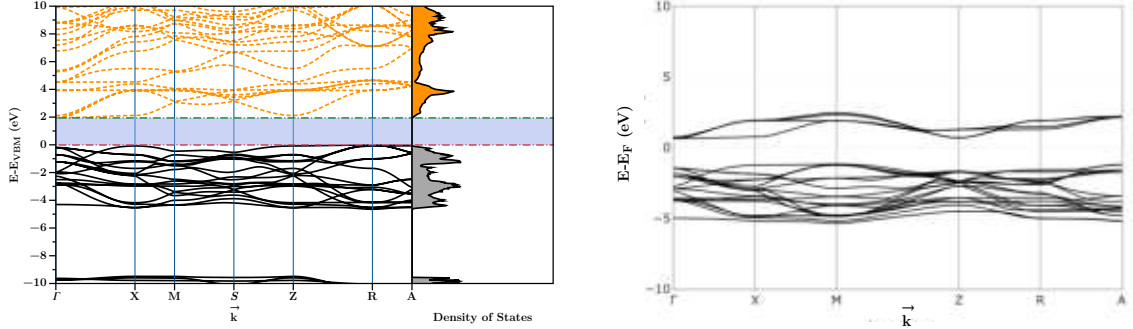


**Figure 4.3:** Left - Band structure calculated with the plane waves PW method. Right - Band structure calculated with the GTO basis set.

Instead, the direct $\Gamma{\rightarrow}\Gamma$ gaps are found to be 2.15 eV in PW and 1.97 eV for GTO, respectively. The energy difference can be related to the two computational method employed and the used basis set. This is important to consider when comparing similar results.

## 4.1.2 Density of States

The computational investigation performed via DOS analysis of the system shows that the use of the GGA *vs.* hybrid PBE0 functional, as already demonstrated for the unit cell of $BaTiO_3$, opens the gap up. A gap of 1.96 eV and 1.78 eV is found at PBE level for the PW and GTO methods, respectively, while using the PBE0 a gap of 3.57 eV and 3.65 eV can be reported. The values obtained at a hybrid level of theory are in agreement with respect to literature[65], this one obtained at B3LYP level, of 3.73 eV. The atom-resolved DOS
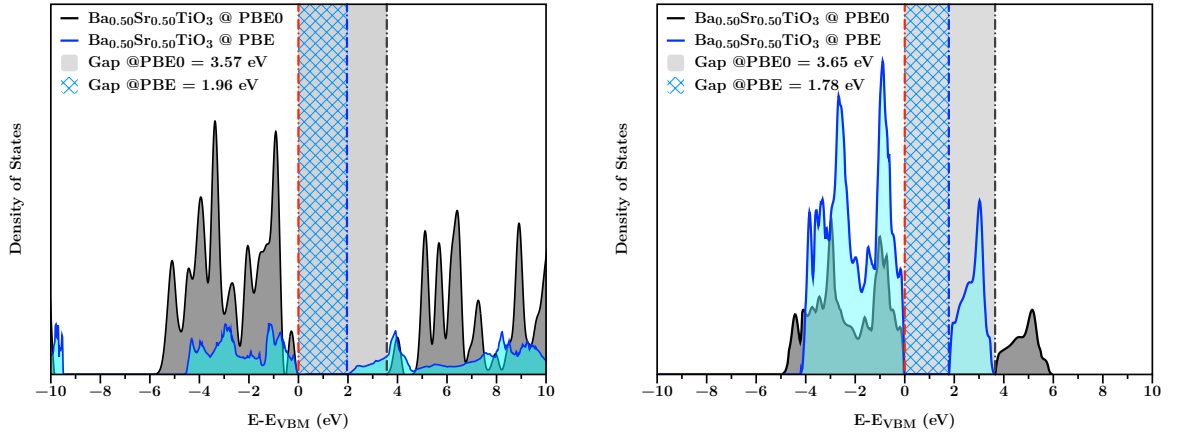


**Figure 4.4:** Left - DOS calculated at PBE and PBE0 level of theory with PW. Right - DOS calculated at PBE and PBE0 level of theory with GTO. In both cases the blue line and grid highlight the PBE DOS and the corresponding gap; the same happens for the black line and grey area, which instead put in evidence the PBE0 DOS and corresponding gap.
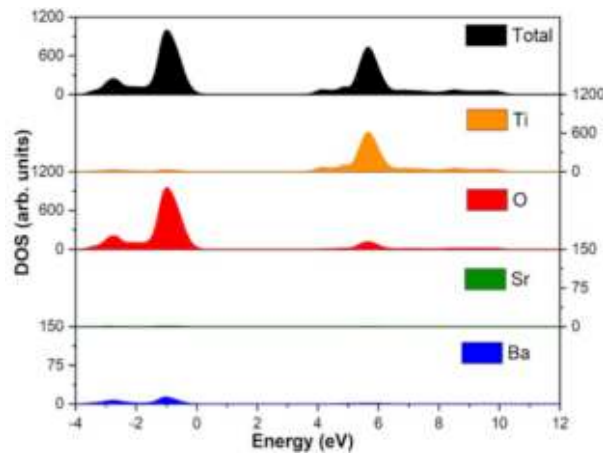


**Figure 4.5:** Atom-resolved DOS for the BTO system[65].

from Oliveira and co-workers[65], see fig. 4.5, clearly shows that contribution to the energy levels of Sr is found at deeper energy levels which in general have little to no influence on the valence band. The VBM and CBM are mainly generated by the $2p$ and $3d$ orbitals of O and Ti atomic species, as already reported in the case of pristine BTO. The key point to keep in mind here is that, despite the little influence at the electronic level that Sr displays, structurally its presence might have an important repercussion, especially with respect to the bulk properties of the system that here are not considered.

## 4.2   $\mathbf{BaTi_{(0.50)}Sn_{(0.50)}O_3}$

Similarly to the previous case, the substitution of one $Ti^{4+}$ with one $Sn^{4+}$ at 50% is of interest for the assessment of the computational methodology. The system optimized at PBE levels both with PW and GTO basis set are reported in fig. 4.6. As found in the case of the $Ba_{(0.5)}Sr_{(0.5)}TiO_3$, the GTO bond distances are found to be larger with respect to the PW calculated ones, with a general trend that oscillates between 5.0 to 7.6%. The
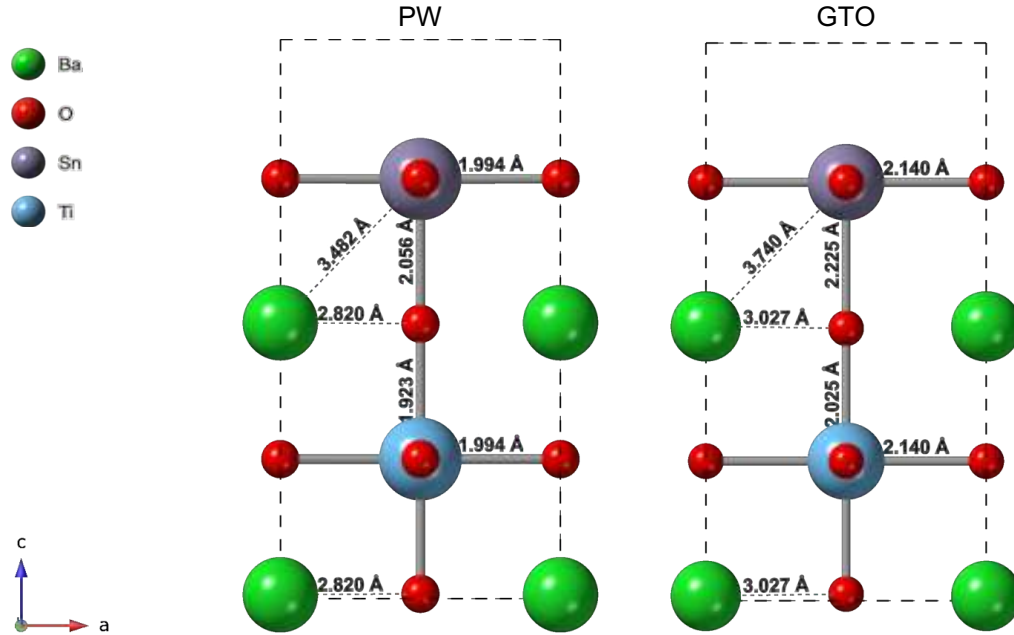


**Figure 4.6:** Plane waves (PW) and Gaussian Type Orbitals (GTO) optimized structures of the 1x1x2 supercell of $BaTi_{(0.5)}Sn_{(0.5)}TiO_3$.

list of the most important bond distances and corresponding percentual errors[2] that can drive the characterization of the doped system are reported in table 4.3. At first, it can be noticed that in both PW and GTO structures the oxygen bonds perpendicular to $Sn^{4+}$ atom and connecting to the following $Ti^{4+}$ tend to get stretched with respect to the ones not directly linked to Sn. This structural modification induces the formation of $SnO_6$ clusters with larger volume of the titanium-based ones. The expansion of the cell can be ascribed to the difference in the atomic radius between $Sn^{4+}$ and $Ti^{4+}$, being equal to 0.690 Å and 0.605 Å, respectively.

---

[2]   The percentual error is estimated as

$$\frac{(GTO\ value - PW\ Value)}{PW\ Value}$$

**Table 4.3:** Comparative table of the most important bond distances obtained by using PW and GTO methods and corresponding percentual errors

| Bonds | PW (Å) | GTO (Å) | PE (%) |
|-------|--------|---------|--------|
| Ti-O  | 1.994  | 2.140   | 7.322  |
| Ti-O  | 1.923  | 2.025   | 5.304  |
| Sn-O  | 1.994  | 2.140   | 7.322  |
| Sn-O  | 2.056  | 2.225   | 8.220  |
| Ba-O  | 2.820  | 3.027   | 7.340  |
| Ba-Sn | 3.482  | 3.740   | 7.410  |

## 4.2.1 Band Structure

The band structure analysis of the $BaTi_{0.50}Sn_{0.50}O_3$ reveals a more complex interplay of the energy levels with respect to the strontium doped one. This is partially caused by the potential localization of the $4d$ orbitals of the Sn on the conduction band, as highlighted from literature[65]. At a careful inspection of the band structures plots, fig. 4.7, for the
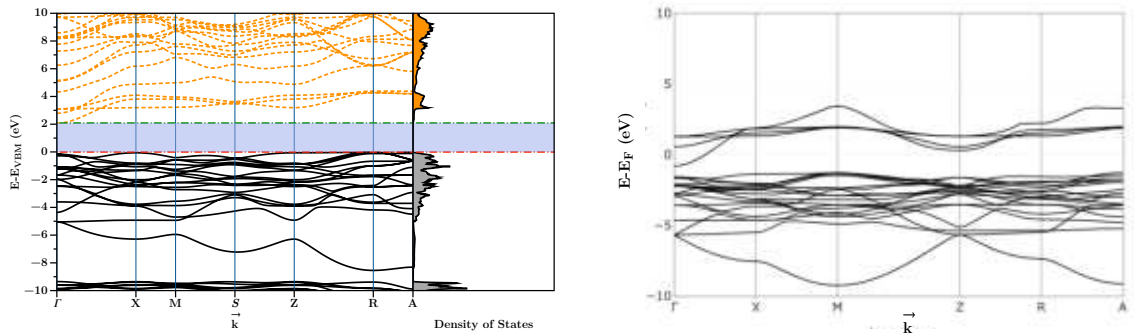


**Figure 4.7:** Left - Band structure calculated with the plane waves PW method. Right - Band structure calculated with the GTO basis set.

CBM $\Gamma$-$X$ for both the Sr- and Sn-doped systems at 50%, it can be noticed that while for the former case the band is practically flat, on the latter it has a quasi-parabolic shape. Based on the relation between the effective mass of the charge carries and band curvature, in first approximation it can be speculated that the electron-hole recombination is more effective in the Sn-doped system rather than in the Sr-doped one[65]. This is due to the fact that a broader band induces a larger effective masses and, in turn, reduces the charge-carrier mobility, while a highly-localized minimum point can reduce the effective mass and hence, increase the mobility. As such, the different shapes of the CBM of the Sn- and Sr-doped systems can already at this preliminary stage of the study suggest which of the two (Sn-doped) is more likely to be a promising material for electron-optical application. The indirect gaps of the two systems are found for $R$-$\Gamma$ = 2.07 eV in the case of PW and $M$-$\Gamma$ = 2.05 eV in the case of the GTO one, meanwhile the $\Gamma$-$\Gamma$ gap reported for both the system is equal to 2.24 eV for PW and 2.34 eV for GTO. The indirect gaps are found at different high-symmetry points like in the Sr-doped case because, while in the PW system the path is manually set throughout a punctual selection of the $\vec{k}$-points in the reciprocal space, in the GTO software, once defined the points, they are mapped with respect to

tabulated data which might slightly differ. In turn, the information that is provided in both cases is the same, and as usual, the comparison is for qualitative purposes.

## 4.2.2 Density of States

Similarly to the Sr-doped system at 50%, the BaTi$_{(0.50)}$Sn$_{(0.50)}$O$_3$ DOS comparison between PBE and PBE0 functionals highlights the impact that the level of theory can have on the determination of the electronic properties of this class of complex systems, see fig. 4.8. In particular, the PBE0 gap in both cases differs of 0.04 eV, being the gap with PW at PBE0 equal to 3.81 eV and with GTO 3.85 eV, respectively.
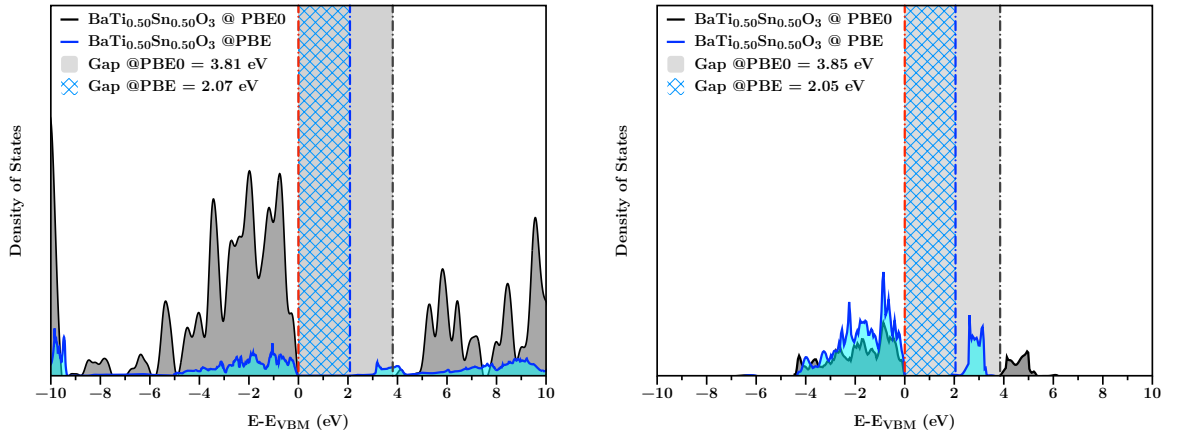


**Figure 4.8:** Left - DOS calculated at PBE and PBE0 level of theory with PW. Right - DOS calculated at PBE and PBE0 level of theory with GTO. In both cases the blue line and grid highlight the PBE DOS and the corresponding gap; the same happens for the black line and grey area, which instead put in evidence the PBE0 DOS and corresponding gap.
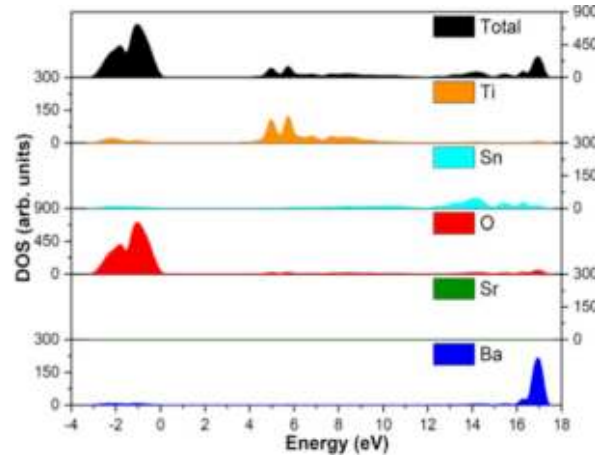


**Figure 4.9:** Atom-resolved DOS for the Sn-doped system[65].

The single contributions to the DOS have been previously investigated for a similar system presented here, where also the strontium atom is accounted at the same time. The atom-resolved projection on the DOS in fig. 4.9 shows that, first of all, Sr does not practically contribute in any case to the valence and conduction bands at all, having only a minor effect on the core electrons. The conclusions derived on the previous section for the Sr-doped BaTiO$_3$ system at 50% are still valid in this case. Interestingly, it can be observed that tin has instead a non-negligible contribution in the conduction band in particular,

thus corroborating the analysis done for its direct influence on the resulting band structure of the system.

# 4.3   $\mathbf{Ba}_{(0.75)}\mathbf{Sr}_{(0.25)}\mathbf{TiO}_3$

The study of models at high doping percentages as presented till now is helpful to set the bases on top of which more realistic models can be built. This is the case for both Sr- and Sn-doped systems presented till now. While in the previous sections the limiting cases for 50% doping was reported, now more realistic structures are going to be presented and their structural and electronic properties discussed. Following the same order of appearance, in this section the BaTiO$_3$ doped at 25% with Sr is reported, see fig. 4.10. To achieved this stoichiometric substitution, a supercell propagated along the $b$ and $c$ axis is performed (1x2x2), starting from the corresponding optimized BaTiO$_3$ unit cell, both for PW and GTO. The resulting supercells feature four Ti$^{4+}$ atoms which are six-coordinated, while both Ba$^{2+}$ and Sr$^{2+}$ are twelve-coordinated. The two supercells, once operated the Sr $\rightarrow$
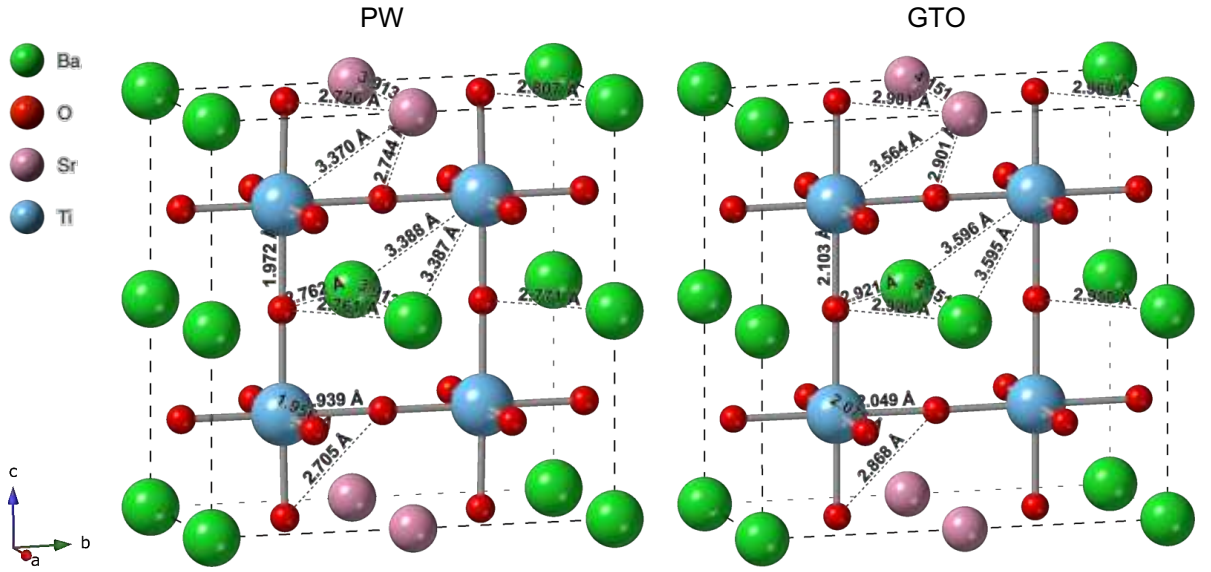


**Figure 4.10:** Plane waves (PW) and Gaussian Type Orbitals (GTO) optimized structures of the 1x2x2 supercell of Ba$_{(0.75)}$Sr$_{(0.25)}$TiO$_3$.

Ba substitution, have been re-optimized preserving their symmetry. The results show that, reflecting the 50% doping case, for the GTO larger bonds are obtained, with optimized cell parameters of $a = 4.14$ Å and $b = c = 8.30$ Å with GTO, while for PW $a = 3.91$ Å and $b = c = 7.83$ Å, confirming the tendency that has already been demonstrated above, that GTO generally displays structural values that are 5-6% larger than PW. The two structures with the most important bond distances are reported in table 4.4. with the correspoding percentual errors[3]. The Sr-O bonds in PW is 2.726 Å and 2.744 Å, while in GTO they are 2.901 Å in both cases, highlighting that PW is more sensitive to the local surrounding environment with respect to GTO. This is very important when considering the local modifications that doping atomic species or defects can have on the resulting cluster. The average difference between the PW and GTO methods is found to be around 6.0%, in line with previous analysis reported in this work. One of the most important conclusions on the structural investigation of the 25% substitution of Sr atom in BaTiO$_3$

---

[3]   The percentual error is estimated as

$$\frac{\text{(GTO value} - \text{PW Value)}}{\text{PW Value}}$$

**Table 4.4:** Comparative table of the most important bond distances obtained by using PW and GTO methods and corresponding percentual errors. Not all bonds highlighted in are listed in the following table, only the most relevant ones.

| Bonds | PW (Å) | GTO (Å) | PE (%) |
|-------|------|-------|-------|
| Ti-O  | 1.956 | 2.075 | 6.084 |
| Ti-O  | 1.939 | 2.049 | 5.673 |
| Ti-O  | 1.972 | 2.103 | 6.643 |
| Ti-Ba | 3.387 | 3.595 | 6.141 |
| Ti-Ba | 3.388 | 3.596 | 6.139 |
| Ba-O  | 2.761 | 2.920 | 5.759 |
| Ba-O  | 2.762 | 2.921 | 5.757 |
| Sr-O  | 2.744 | 2.901 | 5.722 |
| Sr-O  | 2.726 | 2.901 | 6.420 |
| Sr-Ti | 3.370 | 3.564 | 5.757 |
| Sr-Sr | 3.913 | 4.151 | 6.082 |

is the generation of localized clusters of $SrO_{12}$ which might are depicted by the Sr-O bonds in PW, while for the GTO case this is less obvious at a first inspection. However, the compression of the Sr-cluster in GTO system can be equally deduced by the general decrease of the bond length between Ba-Ti with respect to Sr-Ti.

## 4.3.1 Band Structure

The band structure of the Ba$_{(0.75)}$Sr$_{(0.25)}$TiO$_3$ presents more complex bands population with respect to the previous cases, this due to the increasing number of atoms required to generate the supercell. Despite this, it can still be recognized the same band distribution around the gap, specifically for the VBM and CBM. While the same coordinates for the $\vec{k}$-path are maintained, obviously the reciprocal structure of the system is different and, in turn, the reference for the indirect band gap. In fact, in this case, analyzing the PW band structure, it can be found that the indirect band gap changed from $R{\rightarrow}\Gamma$ to $Z{\rightarrow}\Gamma$, with a corresponding value of 1.98 eV. The same happens to the GTO case, where the indirect gap moved from $M{\rightarrow}\Gamma$ to $X{\rightarrow}\Gamma$, whose corresponding value is 1.79 eV. The
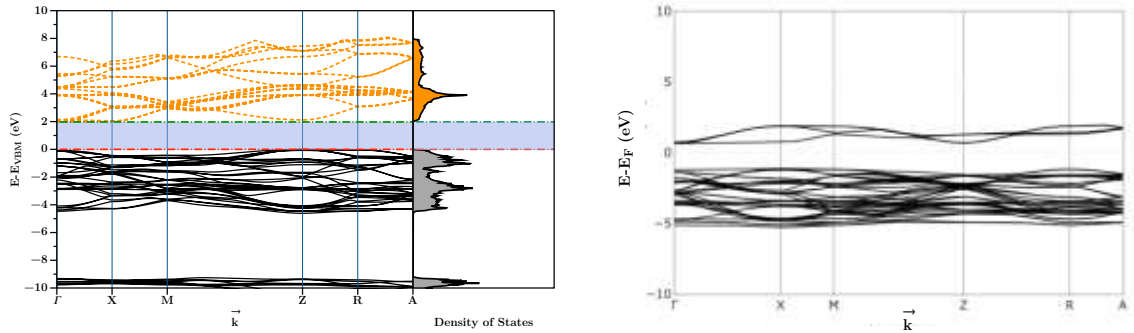


**Figure 4.11:** Left - Band structure calculated with the plane waves PW method. Right - Band structure calculated with the GTO basis set.

direct $\Gamma{\rightarrow}\Gamma$ gaps of the two systems are, at PBE level, 2.15 eV and 1.87 eV, respectively. The composition of the bands, like for the 50% case, can be ascribed to the $3d$ of Ti and $2p$ orbitals of the O, with a contribution coming from the Sr atom that is likely to be hidden deeper in the energy levels. However, the careful analysis of the $\Gamma{\rightarrow}X$ segment of the two band structures plot shows that, in both cases, the CBM is almost flat. This is in line with what discussed before comparing the Sr- *vs*. Sn-doped systems for the 1x1x2 supercell. This feature is found also at lower content of Sr, that is, it might be expected that also at these levels of doping the mobility of the charge carriers is lower if compared to Sn-doped systems. Nonetheless, the 25% presence of Sr can still show promising structural modifications enhancing the general performances of the systems. With this regards, in the next future the study of the dielectric properties will also be performed and compared with experimental values, if available, in order to better depict pros and cons of such material.

## 4.3.2 Density of States

The analysis of the density of states performed at PBE and PBE0 levels of theory shows that, like in the previously reported cases, the hybrid functional open the gap up with respect to the GGA approximation, see fig. 4.12. The estimate of the gaps at a hybrid levels shows a certain mismatch between the two approaches here employed, namely PW and GTO, appears. Specifically, it is shown that, for the 25% Sr doping of BTO, the PW-PBE0 method predicts a gap of 4.69 eV, while in the GTO case of 3.65 eV. This mismatch can be related to the problems encountered during the simulation of the PW data, possibly related to the integration grid used with the $\vec{k}$-point. Further investigations are already planned to solve this issue. Conversely, the PBE0 gap found with the GTO-based method provides a gap that is more aligned with those previously found, at around 3.65 eV.
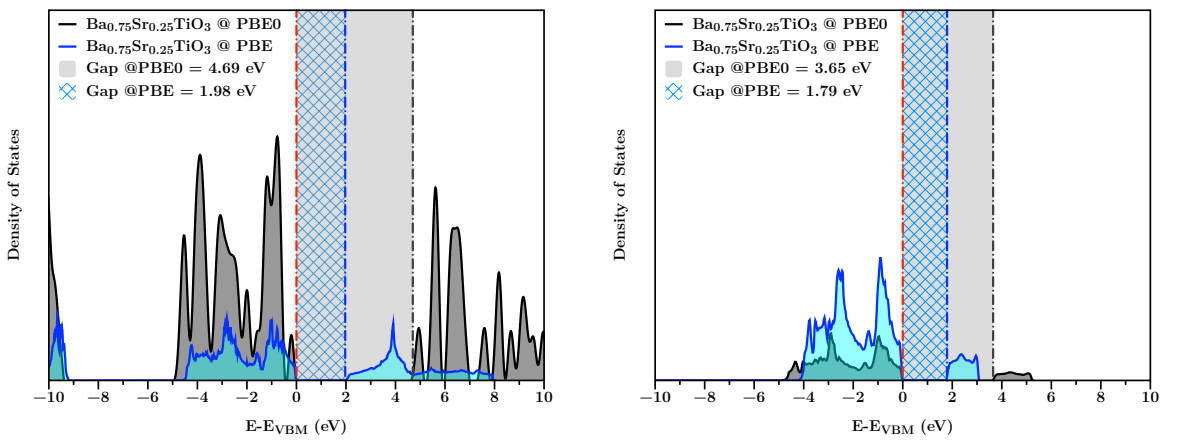


**Figure 4.12:** Left - DOS calculated at PBE and PBE0 level of theory with PW. Right - DOS calculated at PBE and PBE0 level of theory with GTO. In both cases the blue line and grid highlight the PBE DOS and the corresponding gap; the same happens for the black line and grey area, which instead put in evidence the PBE0 DOS and corresponding gap.

Once more, it was not possibile to distinguish the atom-resolved contributions to the states due to some limitations in the codes used, however, the data previously reported fig. 4.5, can still operate as qualitative guide for the correct interpretation of the total DOS. Because of a more relative presence of Ti and O atoms in a 1x2x2 supercell compare with Sr, then their contribution to the bands, as discussed in the previous section, becomes predominant. That is, the $3d$ orbitals of Ti partially hybridize with the $2p$ orbitals of the O, populating the VBM and CBM. As it might be expected by also investigating systems with higher content of Sr, the contribution of this atomic species to DOS is practically negligible, even more at lower doping percentages.

# 4.4 BaTi$_{(0.75)}$Sn$_{(0.25)}$O$_3$

Finally, the last structure analyzed in the benchmarking work presented here is the 1x2x2 supercell of BaTiO$_3$ doped at 25% with Sn$^{4+}$, see fig. 4.13. Like for the previous case, an expansion of the optimized unit cell of BTO is first performed, followed by the substitution of one Sn→Ti, which replaces the center of one of the octahedral clusters forming in the supercell. The supercells are then optimized in order to minimize the interatomic forces, as reported in fig. 4.13. The optimized lattice parameters are $a = 3.96$ Å with $b = c = 7.91$ Å in the PW case and $a = 4.24$ Å with $b = c = 8.44$ Å in the GTO case, confirming the systematic difference between the two methods. The comparative table 4.5, with
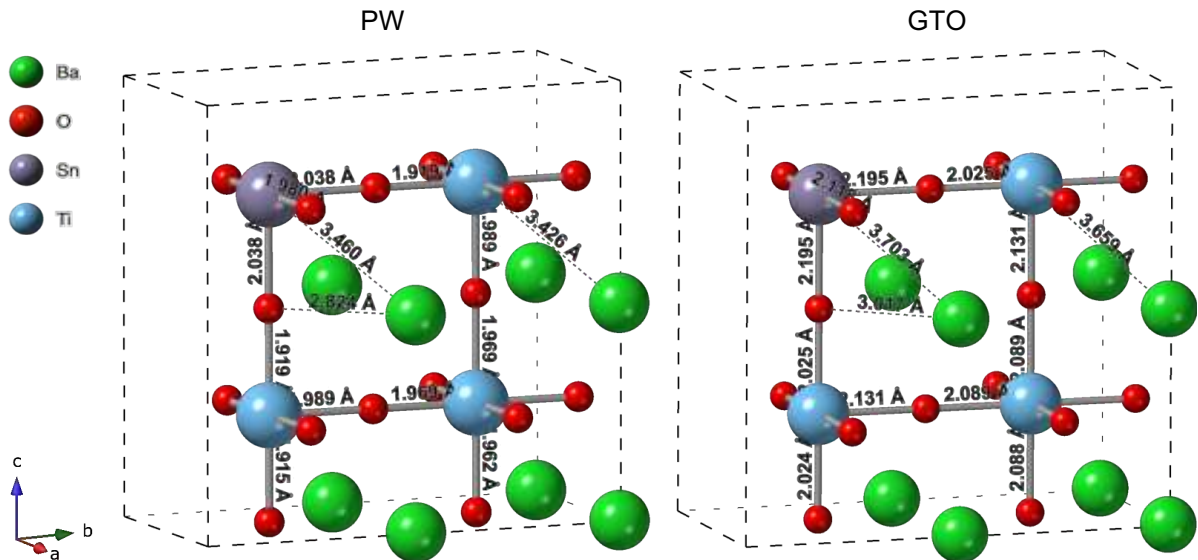


**Figure 4.13:** Plane waves (PW) and Gaussian Type Orbitals (GTO) optimized structures of the 1x2x2 supercell of BaTi$_{(0.75)}$Sn$_{(0.25)}$O$_3$.

percentual error[4] difference between the plane waves and GTO approaches, highlights that in the surrounding of the Sn$^{4+}$ atom a general elongation of the bonds occurs, as already noticed in the 50% doped supercells. This is even more appreaciable when comparing the shared oxygen atom between Ti and Sn, which is pulled towards Ti. This phenomenon is also affecting other nearby atoms like Ba. So, contrary to the case of Sr, the effect of doping with tin generates an expanded octahedral cluster where Sn finds itself to be 6-coordinated. The most intuitive reason for this structural modification is the ionic radius difference that is featured by Sn with respect to Ti, the first being equal to 0.690 Å while the second 0.605 Å.

---

[4] The percentual error is estimated as

$$\frac{(\text{GTO value} - \text{PW Value})}{\text{PW Value}}$$

**Table 4.5:** Comparative table of the most important bond distances obtained by using PW and GTO methods and corresponding percentual errors. Not all bonds highlighted in are listed in the following table, only the most relevant ones.

| Bonds | PW (Å) | GTO (Å) | PE (%) |
|---|---|---|---|
| Ti-O | 1.915 | 2.024 | 5.692 |
| Ti-O | 1.919 | 2.025 | 5.524 |
| Ti-O | 1.989 | 2.131 | 7.139 |
| Ti-O | 1.969 | 2.089 | 6.094 |
| Ti-Ba | 3.426 | 3.659 | 6.801 |
| Ba-O | 2.824 | 3.017 | 6.834 |
| Sn-O | 2.038 | 2.195 | 7.704 |
| Sn-O | 1.980 | 2.1185 | 7.020 |
| Sn-Ba | 3.460 | 3.703 | 7.023 |

## 4.4.1 Band Structure

Similarly to the 25% Sr doped system, the band structure plot of the BaTi$_{(0.75)}$Sn$_{(0.25)}$O$_3$ system at PW and GTO features an indirect gap that is found to be $Z \rightarrow \Gamma$ for the PW case, while it is $X \rightarrow \Gamma$ for the GTO one, see fig. 4.14. The corresponding values are 2.07 eV in the first case and 1.26 eV in the second, with a large discrepancy at PBE level of theory. This difference will be further investigated in the future, refining the calculation in order to minimize the energy gap difference. The $\Gamma \rightarrow \Gamma$ gap is instead equal to 2.13 eV with PW and 1.34 eV with GTO.
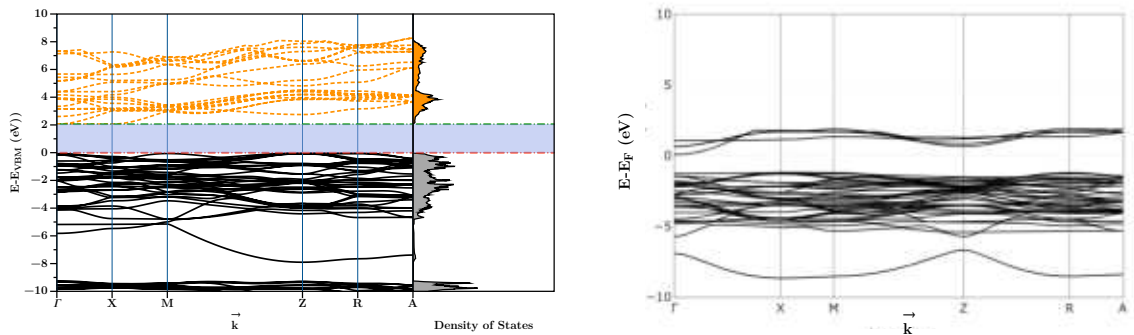


**Figure 4.14:** Left - Band structure calculated with the plane waves PW method. Right - Band structure calculated with the GTO basis set.

By inspecting the gaps values reported above it might be deduced that a sort of systematic shift is present between the two computational approaches employed. Nonetheless, it is has also to be considered that tiny structural differences might have a large impact on the resulting electronic structure. This particular aspect is going to be further investigated in the next future. Another key point that will be elucidate in the future for this system is the nature of the CBM structure, *i.e.*, the difference that is found *w.r.t.* 50% content at the PW level. In fact, while in the higher Sn content the $X \rightarrow \Gamma$ section of the CBM was found to show a rather well localized structure, in this case it is flat, resembling the Sr

doping. This behavior is slightly less clear in the GTO case, which instead shows a rather intermediate situation. However, from these bands plot it is not possible to conclude, like in the 50% case of Sn$^{4+}$, that the system will favor charge carrier mobility.

## 4.4.2  Density of States

The study of the density of states of the BaTi$_{(0.75)}$Sn$_{(0.25)}$O$_3$ shows that in both PW and GTO cases the PBE0 results to have a major influence on the gap opening, thus fostering the conclusion that the system is an insulator, see fig. 4.15. In particular, the PBE0 gaps are found to be more or less in agreement, differently from the previous case of the 25% of Sr-doped structure, with a value of 3.84 eV for PW and 3.54 eV for GTO. Despite the
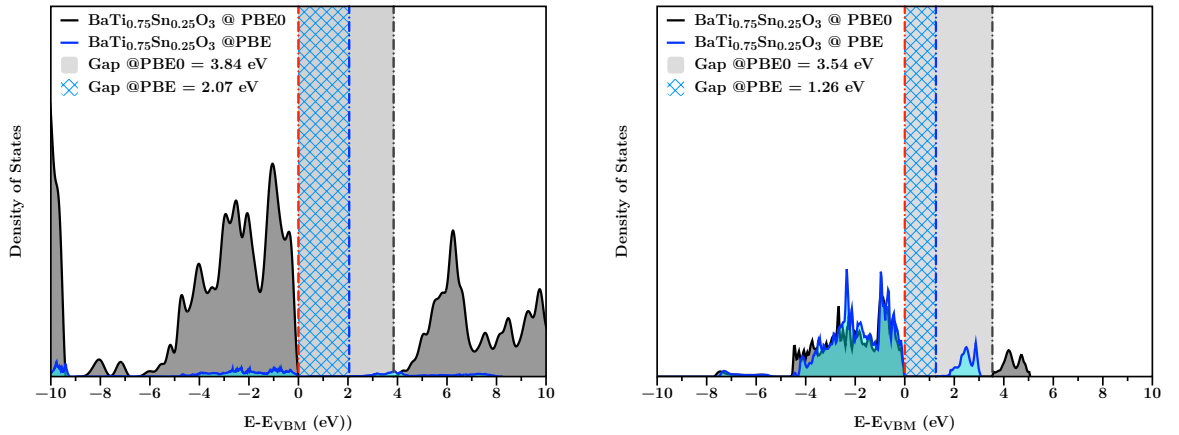


**Figure 4.15:** Left - DOS calculated at PBE and PBE0 level of theory with PW. Right - DOS calculated at PBE and PBE0 level of theory with GTO. In both cases the blue line and grid highlight the PBE DOS and the corresponding gap; the same happens for the black line and grey area, which instead put in evidence the PBE0 DOS and corresponding gap.

relatively low content of tin in the system, by comparing with atom-resolved DOS reported in fig. 4.9, it can be deduced that a small amount to the CBM can be derived from the tin atom, combined with orbital contributions from oxygen and titanium. A more detailed analysis of the single contribution will help to further elucidate the role that each atomic species has and how the doping percentage operate in this sense.

# Chapter 5

# Conclusions and Future Challenges

In conclusion, in this explorative work two computational methodologies, both based on density functional theory (DFT) approach, have been used and applied to the same set of systems, comparing structural and electronic properties of the same. Namely, the pristine $BaTiO_3$ system, $Ba_{(x)}Sr_{(1-x)}TiO_3$ at 25% and 50% and $BaTi_{(x)}Sn_{(1-x)}O_3$ at 25% and 50%, where the doping atomic species are strontium and tin, respectively, has been investigated. While in one case the Plane Waves (PW) basis set is employed, in the other case the Gaussian Type Orbitals (GTO) basis set is used. The major differences that are consistent throughout the whole study is the persistent overestimation, with respect to PW, of the GTO optimized structural parameters, set around 6%. This is partially due to the actual definition of the atomic species, and in particular the valence electron shells. Nonetheless, starting from the study of the pristine $BaTiO_3$, it can be assessed that the two methods are consistent and both reproduce with high fidelity the band structure and corresponding density of states (DOS), also compared with literatures data. First, the study of the 1x1x2 supercells for both strontium and tin substituted systems at 50%, and then of the 1x2x2 supercells with the same doping atomic species at 25% of stoichiometric content, highlights the general differences between the two approaches. Namely, the formation of $[SrO_{12}]$ and $[SnO_6]$ clusters within the doped supercells is not always clear if not by a careful inspection of the bonds surrounding the doping atom. The GTO method is shown to systematically lead to larger bonds values with respect to PW. The electronic structure analysis instead is more involved, since moving from the 1x1x1 $\rightarrow$ 1x1x2 $\rightarrow$ 1x2x2 supercells needs to account for a resampling of the reciprocal space. In this sense some discrepancies are noticed between PW and GTO. However, within the same method and within the same structure considered, it can be found that, the $BaTiO_3$ unit cell displays indirect gap at $M{\rightarrow}\Gamma$ and $R{\rightarrow}\Gamma$, for both PW and GTO. Meanwhile, for the 1x1x2 supercells, it is found that the preferential path for the indirect gap is $R{\rightarrow}\Gamma$ for PW and $M{\rightarrow}\Gamma$ for GTO. Finally, in the case of the 1x2x2 system, the indirect gap is found at $Z{\rightarrow}\Gamma$ for PW and $X{\rightarrow}\Gamma$ for GTO. The calculation of the corresponding density of states for each structures are, for the majority of the cases, in agreement among them, providing a gap, both for the PBE and PBE0 functionals, in line with literatures data. Only in the 25% Sr-doping case, the gap found in the corresponding DOS is quite large (4.69 eV) at PBE0 level of theory as obtained with the PW method, while the one obtained at the same level of theory with GTO is 3.85 eV. These discrepancies will be further investigated in the next future in order to sort them out and rationalize the behavior. This explorative work is the starting point for future studies, partly of which are already ongoing, to investigate in details the structural and electronic properties of $ABO_3$ doped systems.

# Bibliography

[1] C. Randall, R. Newnham, and L. Cross, "History of the first ferroelectric oxide, batio3," *Materials Research Institute, The Pennsylvania State University, University Park, Pa, USA*, vol. 1, 2004.

[2] H. Thurnaurer and J. Deaderick, U.S. Patent No. 2,429,588, Oct. 21, 1947; filed (1941).

[3] A. Von Hippel, R. Breckenridge, F. Chesley, and L. Tisza, "High dielectric constant ceramics," *Industrial & Engineering Chemistry*, vol. 38, no. 11, pp. 1097–1109, 1946.

[4] B. Wul and J. Goldman, "Ferroelectric switching in batio3 ceramics," *CR Acad Sci URSS*, vol. 51, p. 21, 1946.

[5] H. D. Megaw, "Crystal structure of barium titanate," *Nature*, vol. 155, no. 3938, pp. 484–485, 1945.

[6] H. F. Kay and P. Vousden, "Xcv. symmetry changes in barium titanate at low temperatures and their relation to its ferroelectric properties," *The London, Edinburgh, and Dublin Philosophical Magazine and Journal of Science*, vol. 40, no. 309, pp. 1019–1040, 1949.

[7] S. Miyake and R. Ueda, "On polymorphic change of batio3," *Journal of the Physical Society of Japan*, vol. 1, no. 1, pp. 32–33, 1932.

[8] R.B.Gray, U.S.Patent No.2, 486, 560, Nov.1 (1949);filed in 1946.

[9] A. F. Devonshire, "Xcvi. theory of barium titanate: Part i," *The London, Edinburgh, and Dublin Philosophical Magazine and Journal of Science*, vol. 40, no. 309, pp. 1040–1063, 1949.

[10] A. Devonshire, "Cix. theory of barium titanate—part ii," *The London, Edinburgh, and Dublin Philosophical Magazine and Journal of Science*, vol. 42, no. 333, pp. 1065–1079, 1951.

[11] V. L. Ginzburg, "Phase transitions in ferroelectrics: some historical remarks," *Physics-Uspekhi*, vol. 44, no. 10, p. 1037, 2001.

[12] L. Landau and E. Lifshitz, "On the theory of the dispersion of magnetic permeability in ferromagnetic bodies," in *Perspectives in Theoretical Physics*, pp. 51–65, Elsevier, 1992.

[13] M. McQuarrie and F. W. Behnke, "Structural and dielectric studies in the system (ba, ca)(ti, zr) o3," *Journal of the American Ceramic Society*, vol. 37, no. 11, pp. 539–543, 1954.

[14] W. W. Coffeen, "Dielectric bodies in the quaternary system batio3–basno3–srsno3–casno3," *Journal of the American Ceramic Society*, vol. 36, no. 7, pp. 215–221, 1953.

[15] M. Acosta, N. Novak, V. Rojas, S. Patel, R. Vaish, J. Koruza, G. Rossetti Jr, and J. Rödel, "Batio3-based piezoelectrics: Fundamentals, current status, and perspectives," *Applied Physics Reviews*, vol. 4, no. 4, p. 041305, 2017.

[16] P. Hohenberg and W. Kohn, "Physical review, 136," *B864*, 1964.

[17] L. H. Thomas, "The calculation of atomic fields," *Mathematical Proceedings of the Cambridge Philosophical Society*, vol. 23, no. 5, p. 542–548, 1927.

[18] E. Fermi, "A statistical method for the determination of some priorieta dell'atome," *Rend. Accad. Nat. Lincei*, vol. 6, no. 602-607, p. 32, 1927.

[19] W. Kohn and L. J. Sham, "Self-consistent equations including exchange and correlation effects," *Physical review*, vol. 140, no. 4A, p. A1133, 1965.

[20] D. M. Ceperley and B. J. Alder, "Ground state of the electron gas by a stochastic method," *Physical review letters*, vol. 45, no. 7, p. 566, 1980.

[21] G. Ortiz and P. Ballone, "Correlation energy, structure factor, radial distribution function, and momentum distribution of the spin-polarized uniform electron gas," *Physical Review B*, vol. 50, no. 3, p. 1391, 1994.

[22] E. Wigner, "On the interaction of electrons in metals," *Physical Review*, vol. 46, no. 11, p. 1002, 1934.

[23] J. P. Perdew, J. A. Chevary, S. H. Vosko, K. A. Jackson, M. R. Pederson, D. J. Singh, and C. Fiolhais, "Atoms, molecules, solids, and surfaces: Applications of the generalized gradient approximation for exchange and correlation," *Physical review B*, vol. 46, no. 11, p. 6671, 1992.

[24] J. P. Perdew, J. Chevary, S. Vosko, K. A. Jackson, M. R. Pederson, D. Singh, and C. Fiolhais, "Erratum: Atoms, molecules, solids, and surfaces: Applications of the generalized gradient approximation for exchange and correlation," *Physical Review B*, vol. 48, no. 7, p. 4978, 1993.

[25] C. Lee, W. Yang, and R. G. Parr, "Development of the colle-salvetti correlation-energy formula into a functional of the electron density," *Physical review B*, vol. 37, no. 2, p. 785, 1988.

[26] J. P. Perdew and A. Zunger, "Self-interaction correction to density-functional approximations for many-electron systems," *Physical Review B*, vol. 23, no. 10, p. 5048, 1981.

[27] J. P. Perdew, K. Burke, and M. Ernzerhof, "Generalized gradient approximation made simple," *Physical review letters*, vol. 77, no. 18, p. 3865, 1996.

[28] P. J. Stephens, F. J. Devlin, C. F. Chabalowski, and M. J. Frisch, "Ab initio calculation of vibrational absorption and circular dichroism spectra using density functional force fields," *The Journal of physical chemistry*, vol. 98, no. 45, pp. 11623–11627, 1994.

[29] K. Kim and K. Jordan, "Comparison of density functional and mp2 calculations on the water monomer and dimer," *The Journal of Physical Chemistry*, vol. 98, no. 40, pp. 10089–10094, 1994.

[30] J. Reinhold, "The challenge of d and f electrons," *Theory and computation. ACS symposium series*, vol. 394, 1990.

[31] S. H. Vosko, L. Wilk, and M. Nusair, "Accurate spin-dependent electron liquid correlation energies for local spin density calculations: a critical analysis," *Canadian Journal of physics*, vol. 58, no. 8, pp. 1200–1211, 1980.

[32] R. M. Martin, *Electronic structure: basic theory and practical methods*. Cambridge university press, 2020.

[33] D. Hamann, M. Schlüter, and C. Chiang, "Norm-conserving pseudopotentials," *Physical Review Letters*, vol. 43, no. 20, p. 1494, 1979.

[34] D. Vanderbilt, "Soft self-consistent pseudopotentials in a generalized eigenvalue formalism," *Physical review B*, vol. 41, no. 11, p. 7892, 1990.

[35] G. Jansen, "Wiley interdiscip," *Rev.: Comput. Mol. Sci*, vol. 4, no. 127, pp. 10–1002, 2014.

[36] R. S. Mulliken, "Spectroscopy, molecular orbitals, and chemical bonding," *Science*, vol. 157, no. 3784, pp. 13–24, 1967.

[37] J. C. Slater, "Atomic shielding constants," *Physical Review*, vol. 36, no. 1, p. 57, 1930.

[38] P. M. Gill, "Molecular integrals over gaussian basis functions," in *Advances in quantum chemistry*, vol. 25, pp. 141–205, Elsevier, 1994.

[39] L. Fernandez Pacios and P. Christiansen, "Ab initio relativistic effective potentials with spin-orbit operators. i. li through ar," *The Journal of chemical physics*, vol. 82, no. 6, pp. 2664–2671, 1985.

[40] F. Birch, "Finite elastic strain of cubic crystals," *Physical review*, vol. 71, no. 11, p. 809, 1947.

[41] F. Murnaghan, "The compressibility of media under extreme pressures," *Proceedings of the national academy of sciences of the United States of America*, vol. 30, no. 9, p. 244, 1944.

[42] H. Heise, "Infrared and raman spectroscopy," 1995.

[43] P. Giannozzi, S. Baroni, N. Bonini, M. Calandra, R. Car, C. Cavazzoni, D. Ceresoli, G. L. Chiarotti, M. Cococcioni, I. Dabo, A. Dal Corso, S. de Gironcoli, S. Fabris, G. Fratesi, R. Gebauer, U. Gerstmann, C. Gougoussis, A. Kokalj, M. Lazzeri, L. Martin-Samos, N. Marzari, F. Mauri, R. Mazzarello, S. Paolini, A. Pasquarello, L. Paulatto, C. Sbraccia, S. Scandolo, G. Sclauzero, A. P. Seitsonen, A. Smogunov, P. Umari, and R. M. Wentzcovitch, "Quantum espresso: a modular and open-source software project for quantum simulations of materials," *Journal of Physics: Condensed Matter*, vol. 21, no. 39, p. 395502 (19pp), 2009.

[44] P. Giannozzi, O. Andreussi, T. Brumme, O. Bunau, M. B. Nardelli, M. Calandra, R. Car, C. Cavazzoni, D. Ceresoli, M. Cococcioni, N. Colonna, I. Carnimeo, A. D. Corso, S. de Gironcoli, P. Delugas, R. A. D. Jr, A. Ferretti, A. Floris, G. Fratesi, G. Fugallo, R. Gebauer, U. Gerstmann, F. Giustino, T. Gorni, J. Jia, M. Kawamura, H.-Y. Ko, A. Kokalj, E. Küçükbenli, M. Lazzeri, M. Marsili, N. Marzari, F. Mauri, N. L. Nguyen, H.-V. Nguyen, A. O. de-la Roza, L. Paulatto, S. Poncé, D. Rocca, R. Sabatini, B. Santra, M. Schlipf, A. P. Seitsonen, A. Smogunov, I. Timrov, T. Thonhauser, P. Umari, N. Vast, X. Wu, and S. Baroni, "Advanced capabilities for materials modelling with quantum espresso," *Journal of Physics: Condensed Matter*, vol. 29, no. 46, p. 465901, 2017.

[45] R. Dovesi, R. Orlando, A. Erba, C. M. Zicovich-Wilson, B. Civalleri, S. Casassa, L. Maschio, M. Ferrabone, M. De La Pierre, P. d'Arco, *et al.*, "Crystal14: A program for the ab initio investigation of crystalline solids," 2014.

[46] R. Dovesi, V. Saunders, C. Roetti, R. Orlando, C. Zicovich-Wilson, F. Pascale, B. Civalleri, K. Doll, N. Harrison, I. Bush, *et al.*, "Crystal14 user's manual," *University of Torino, Torino*, p. 382, 2014.

[47] X. Zhu, S. Lu, H. Chan, C. Choy, and K. Wong, "Microstructures and dielectric properties of compositionally graded (ba1-xsrx) tio3 thin films prepared by pulsed laser deposition," *Applied Physics A*, vol. 76, no. 2, pp. 225–229, 2003.

[48] P. Giannozzi, O. Andreussi, T. Brumme, O. Bunau, M. B. Nardelli, M. Calandra, R. Car, C. Cavazzoni, D. Ceresoli, M. Cococcioni, *et al.*, "Advanced capabilities for materials modelling with quantum espresso," *Journal of physics: Condensed matter*, vol. 29, no. 46, p. 465901, 2017.

[49] M. Schlipf and F. Gygi, "Optimization algorithm for the generation of oncv pseudopotentials," *Computer Physics Communications*, vol. 196, pp. 36–44, 2015.

[50] J. P. Perdew, M. Ernzerhof, and K. Burke, "Rationale for mixing exact exchange with density functional approximations," *The Journal of chemical physics*, vol. 105, no. 22, pp. 9982–9985, 1996.

[51] C. Adamo and V. Barone, "Toward reliable density functional methods without adjustable parameters: The pbe0 model," *The Journal of chemical physics*, vol. 110, no. 13, pp. 6158–6170, 1999.

[52] G. Sophia, P. Baranek, C. Sarrazin, M. Rérat, and R. Dovesi, "First-principles study of the mechanisms of the pressure-induced dielectric anomalies in ferroelectric perovskites," *Phase Transitions*, vol. 86, no. 11, pp. 1069–1084, 2013.

[53] P. Jeffrey Hay and W. Wadt, "Ab initio effective core potentials for molecular calculations. potentials for the transition metal atoms sc to hg," *J. Chem. Phys*, vol. 82, pp. 270–283, 1985.

[54] M. Frisch, G. Trucks, H. Schlegel, P. Gill, B. Johnson, M. Robb, J. Cheeseman, T. Keith, G. Petersson, J. Montgomery, *et al.*, "Gaussian 94, revision b. 3 gaus-. sian, inc., pittsburgh pa, 1995. ž. 12. wr wadt and pj hay," *J. Chem. Phys*, vol. 82, p. 284, 1985.

[55] R. A. Friesner, R. B. Murphy, M. D. Beachy, M. N. Ringnalda, W. T. Pollard, B. D. Dunietz, and Y. Cao, "Correlated ab initio electronic structure calculations for large molecules," *The Journal of Physical Chemistry A*, vol. 103, no. 13, pp. 1913–1928, 1999.

[56] H. J. Monkhorst and J. D. Pack, "Special points for brillouin-zone integrations," *Physical review B*, vol. 13, no. 12, p. 5188, 1976.

[57] K. Hellwege and A. Hellwege, "Ferroelectrics and related substances, landolt-börnstein, new series," *Group III*, vol. 3, 1969.

[58] J. Wang, F. Meng, X. Ma, M. Xu, and L. Chen, "Lattice, elastic, polarization, and electrostrictive properties of batio 3 from first-principles," *Journal of Applied Physics*, vol. 108, no. 3, p. 034107, 2010.

[59] S. Piskunov, E. Heifets, R. Eglitis, and G. Borstel, "Bulk properties and electronic structure of srtio3, batio3, pbtio3 perovskites: an ab initio hf/dft study," *Computational Materials Science*, vol. 29, no. 2, pp. 165–178, 2004.

[60] M. Uludogan, T. Cagin, and W. A. Goddard, "Ab initio studies on phase behavior of barium titanate," *MRS Online Proceedings Library (OPL)*, vol. 718, 2002.

[61] P. Ghosez, X. Gonze, and J.-P. Michenaud, "First-principles characterization of the four phases of barium titanate," *Ferroelectrics*, vol. 220, no. 1, pp. 1–15, 1999.

[62] H. Chermette, P. Pertosa, and F. Michel-Calendini, "Molecular orbital study of satellites in xps spwctra of batio3 and tio2," *Chemical Physics Letters*, vol. 69, no. 2, pp. 240–245, 1980.

[63] S. Wemple, "Polarization fluctuations and the optical-absorption edge in bati o 3," *Physical Review B*, vol. 2, no. 7, p. 2679, 1970.

[64] R. Dovesi, R. Orlando, B. Civalleri, C. Roetti, V. R. Saunders, and C. M. Zicovich-Wilson, "Crystal: a computational tool for the ab initio study of the electronic properties of crystals," *Zeitschrift für Kristallographie-Crystalline Materials*, vol. 220, no. 5-6, pp. 571–573, 2005.

[65] W. D. Mesquita, S. R. de Jesus, M. C. Oliveira, R. A. P. Ribeiro, M. R. de Cassia Santos, M. G. Junior, E. Longo, and M. F. do Carmo Gurgel, "Barium strontium titanate-based perovskite materials from dft perspective: assessing the structural, electronic, vibrational, dielectric and energetic properties," *Theoretical Chemistry Accounts*, vol. 140, no. 3, pp. 1–12, 2021.

# Acknowledgements